nature medicine

ARTICLES

https://doi.org/10.1038/s41591-018-0223-3

Identification of evolutionarily conserved gene networks mediating neurodegenerative dementia

Vivek Swarup[1,11], Flora I. Hinz[1,11], Jessica E. Rexach[1], Ken-ichi Noguchi[2], Hiroyoshi Toyoshiba[2], Akira Oda[2], Keisuke Hirai[2], Arjun Sarkar[1], Nicholas T. Seyfried[3,4], Chialin Cheng[5], Stephen J. Haggarty[5], International Frontotemporal Dementia Genomics Consortium[6], Murray Grossman[7], Vivianna M. Van Deerlin[8], John Q. Trojanowski[8], James J. Lah[4], Allan I. Levey[4], Shinichi Kondou[2] and Daniel H. Geschwind[1,9,10*]

Identifying the mechanisms through which genetic risk causes dementia is an imperative for new therapeutic development. Here, we apply a multistage, systems biology approach to elucidate the disease mechanisms in frontotemporal dementia. We identify two gene coexpression modules that are preserved in mice harboring mutations in *MAPT*, *GRN* and other dementia mutations on diverse genetic backgrounds. We bridge the species divide via integration with proteomic and transcriptomic data from the human brain to identify evolutionarily conserved, disease-relevant networks. We find that overexpression of miR-203, a hub of a putative regulatory microRNA (miRNA) module, recapitulates mRNA coexpression patterns associated with disease state and induces neuronal cell death, establishing this miRNA as a regulator of neurodegeneration. Using a database of drug-mediated gene expression changes, we identify small molecules that can normalize the disease-associated modules and validate this experimentally. Our results highlight the utility of an integrative, cross-species network approach to drug discovery.

Frontotemporal dementia (FTD) is a highly heritable and common cause of presenile dementia often caused by dominantly acting mutations in the microtubule-associated protein tau (*MAPT*; tau) and in two other genes, granulin precursor (*GRN*) and chromosome 9 open reading frame 72 (*C9orf72*)[1]. Tau pathology is also a core feature of numerous other neurodegenerative syndromes, including Alzheimer's disease (AD) and progressive supranuclear palsy (PSP), and is associated with the pattern of cognitive decline in AD (PSP; for a review see refs [2–4]). Thus, identifying the mechanisms by which tau and other dementia-causing mutations lead to neurodegeneration is of foremost importance in developing new therapies for dementia.

Translating mechanistic studies in mouse models of dementia to human clinical trials has proved challenging[5,6]. We reasoned that one contributing factor, aside from the evolutionary distance between mouse and humans[7], is that common laboratory mouse strains are highly inbred. Although genetic background profoundly affects the biochemical and behavioral repertoires of mouse models of AD[8,9], virtually all studies of neurodegeneration in mice rely on a single inbred strain[10,11].

In this study, we took a multistep systems biology approach to identify robust, human disease-relevant gene networks. To minimize the likelihood that findings were dependent on a single genetic background, we crossed transgenic (Tg) mice harboring the FTD-causing P301S mutation onto three distinct backgrounds and identified early transcriptomic changes observed across mutant F1 progeny, comparing vulnerable regions, such as the cortex and brain stem, to regions less affected in the human tauopathies, such as the cerebellar hemispheres[12]. Through gene network analysis, we identified two major coexpression modules that are conserved across genetic backgrounds and in humans. These modules delineate key pathways deregulated in disease and are differentially enriched for genetic drivers of human FTD, AD and PSP. Using an unbiased integrative genomics approach, we uncovered genome-wide relationships between miRNAs and their biological targets; we experimentally validated these relationships by demonstrating that overexpression of a predicted driver, miR-203, recapitulates the mRNA expression patterns observed with disease and promotes neurodegenerative pathways. As a proof of principle, we also showed that one can leverage these highly conserved coexpression modules to identify tool compounds that mitigate the neurodegeneration induced by miR-203.

Results

We analyzed the F1 offspring resulting from crosses of TPR50 mice expressing the human tau^{P301S} transgene[13] onto FVB, DBA and parent

[1]Program in Neurogenetics, Department of Neurology, David Geffen School of Medicine, University of California, Los Angeles, Los Angeles, CA, USA. [2]CNS Drug Discovery Unit, Pharmaceutical Research Division, Takeda Pharmaceutical Company Limited, Fujisawa, Kanagawa, Japan. [3]Department of Biochemistry, Emory University School of Medicine, Atlanta, GA, USA. [4]Alzheimer's Disease Research Center and Department of Neurology, Emory University School of Medicine, Atlanta, GA, USA. [5]Chemical Neurobiology Laboratory, Center for Genomic Medicine, Massachusetts General Hospital and Harvard Medical School, Boston, MA, USA. [6]A full list of members and affiliations appears at the end of this paper. [7]Center for Neurodegenerative Disease Research, Department of Pathology and Laboratory Medicine, Perelman School of Medicine at the University of Pennsylvania, Philadelphia, PA, USA. [8]The Penn FTD Center, Department of Neurology, Perelman School of Medicine at the University of Pennsylvania, Philadelphia, PA, USA. [9]Department of Human Genetics, David Geffen School of Medicine, University of California, Los Angeles, Los Angeles, CA, USA. [10]Institute of Precision Health, University of California, Los Angeles, Los Angeles, CA, USA. [11]These authors contributed equally to this work: Vivek Swarup, Flora I. Hinz. *e-mail: dhg@mednet.ucla.edu

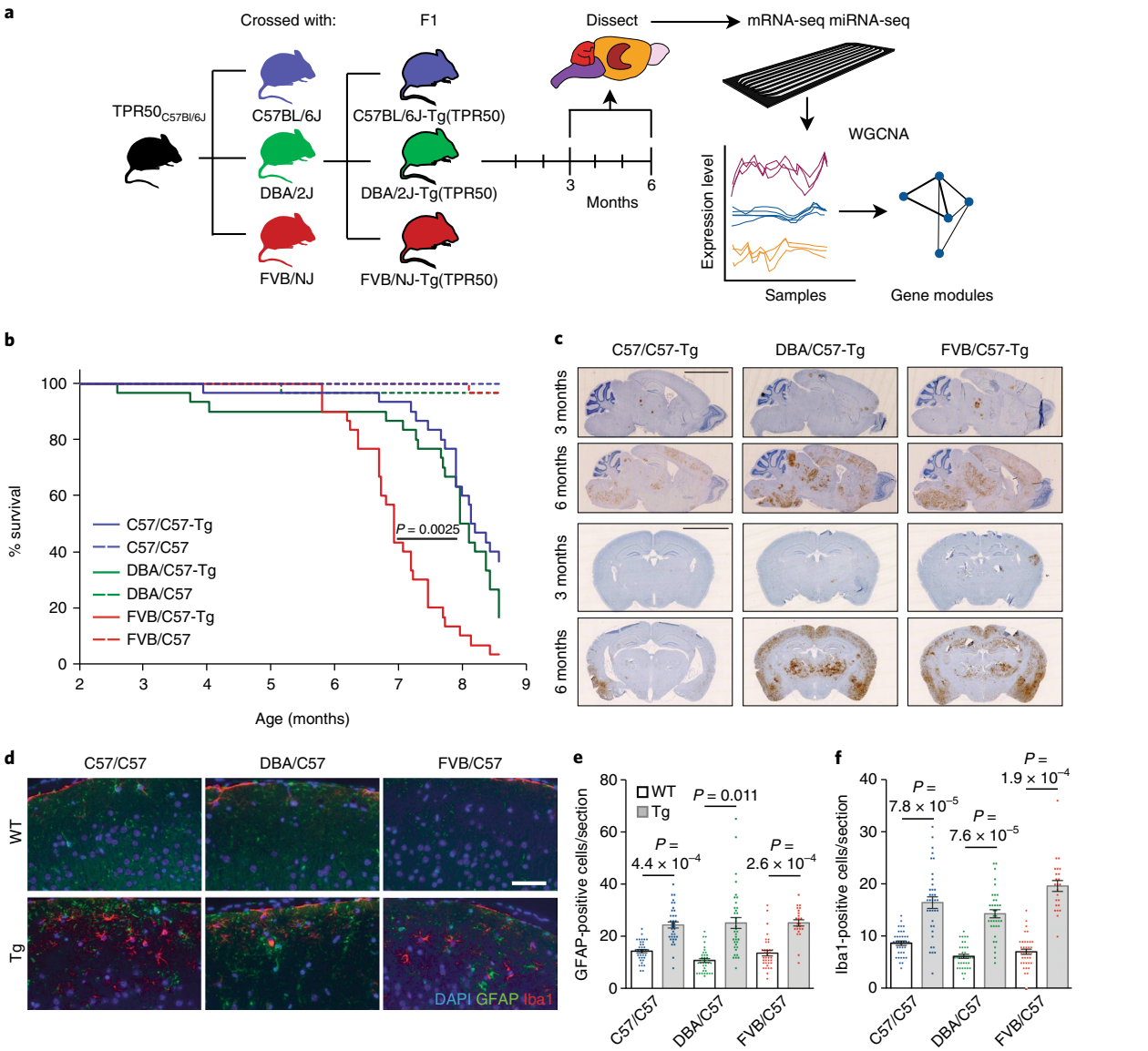

Fig. 1 | Experimental design and characterization of TPR50 tau Tg mice in divergent genetic backgrounds. a, Schematic of the experimental design highlighting that TPR50 mice were crossed with three genetically divergent mouse strains and that tissue from the cortex, hippocampus, brain stem and cerebellum from the resulting F1 crosses was isolated at 3 and 6 months for mRNA-seq, miRNA-seq and downstream WGCNA. **b**, Kaplan–Meier survival curve showing significantly decreased survival of all Tg mice compared to their WT littermates, as well as decreased survival of the FVB/C57-Tg mice compared to DBA/C57-Tg and C57/C57-Tg mice (two-sided log rank test, $P = 0.0025$; $n = 180$, 15 males and 15 females per condition). **c**, Representative images from three independent experiments of phospho-tau-specific AT8 staining and hematoxylin counterstaining in coronal and sagittal brain sections of 3- and 6-month-old Tg mice of all three strains ($n = 4$ mice per group). Sagittal scale bar, 4 µm; coronal scale bar, 3 µm. **d**, Representative images from three independent experiments showing cortical sections of 6-month-old WT and Tg mice of all three strains stained against Iba1 (red) and GFAP (green) and the nuclear counterstain DAPI (blue). Scale bar, 50 µm. **e**,**f**, Quantification of GFAP-positive (**e**) and Iba1-positive (**f**) cells from the cortical slices of 6-month-old mice (unpaired two-tailed *t*-test; $n = 6$ images per mouse, 3 mice per genotype). The center line represents the mean, and error bars show s.e.m.

C57BL/6 lines (Fig. 1a). All three F1 crosses share key features of the disease[13,14], including decreased survival (Fig. 1b) and body weight (Supplementary Fig. 1a,b), progressive accumulation of hyperphosphorylated tau in the cortex and hippocampus (AT8 staining; Fig. 1c), and prominent astrogliosis and microgliosis (Fig. 1d–f). We observed that, consistent with previous reports that FVB mice can be more vulnerable to neurodegeneration, F1 tau^{P301S} Tg mice on the FVB/C57 (TPR50×FVB/NJ) background had decreased survival and increased pathological tau compared with the C57/C57 (TPR50×C57BL/6J) and DBA/C57 (TPR50×DBA/2J) progeny (Fig. 1b and Supplementary Fig. 1c–h). Importantly, no significant decrease in the weight of any of the affected brain areas was detected in Tg animals at 6 months (Supplementary Fig. 1i), consistent with previous data showing no cell loss at this stage[13].

We next investigated whether we could identify a robust, disease-specific transcriptional signature by sampling brain regions varying in disease vulnerability, reasoning that key disease-related gene expression patterns would overlap across affected areas (cortex, hippocampus, brain stem) but would be absent in the cerebellum, which is unaffected[12]. We performed RNA sequencing (RNA-seq) of four brain regions at two time points across the three genetic backgrounds (36 samples per region per time point for a total of

288 RNA-seq samples; Fig. 1a and Methods). The differentially expressed genes from Tg and wild-type (WT) mice clearly separate the tau mutant from WT genotypes within the affected brain regions (Supplementary Fig. 2a–c), but not in the cerebellum (Supplementary Fig. 2a), and are consistent across strains (Supplementary Fig. 2d,e). There was significant overlap in differential expression (Methods and Supplementary Fig. 3a) between the cortex and hippocampus, and there was significant correlation between fold changes in differentially expressed genes (Rank–rank hypergeometric test; $P = 1.0 \times 10^{-409}$) from these two regions ($R^2 = 0.76$, slope = 0.92; Supplementary Fig. 3a). We found lesser, but significant correlation in gene expression between the cortex and brain stem ($R^2 = 0.33$, slope = 0.82; Supplementary Fig. 3a). Consistent with the absence of significant cell loss at 6 months in this model[13], positive regulators of apoptosis (GO:0043065) did not show significant changes across all three strains (Supplementary Fig. 3b–e) and negative regulators of apoptosis (GO:0043066) showed modest, more significant changes (Supplementary Fig. 3f–i). Although we did not observe frank apoptosis, we saw evidence for initial activation of the cellular pathways associated with inflammation in the cerebral cortex by 6 months, including increases in glial fibrillary acidic protein (GFAP) and ionized calcium-binding adapter molecule 1 immunoreactivity in the cortex (Fig. 1d–f).

We observed no significant overlap in gene expression between the cortex and cerebellum (Supplementary Fig. 3j,k) and no correlation between differentially expressed genes in the cortex and cerebellum ($R^2 = 0.01$, slope = 0.14; Supplementary Fig. 3a). Even more striking is that the expression changes of the top upregulated genes in the cerebellum were reversed in the cortex (Supplementary Fig. 3l), implying that protective changes may potentially occur in the cerebellum, as has been previously suggested[12].

Identification of disease-relevant mRNA modules. To place gene expression changes in a systems-level framework, we performed consensus-weighted gene coexpression network analysis (WGCNA[15,16]) across all three heterozygous F1 mouse strains to identify relationships not observed in only a single background (Supplementary Fig. 4a and Supplementary Table 1). We identified four mRNA modules significantly correlated with the transgenic condition in the cortex, which we initially labeled the salmon, turquoise, magenta and pink modules according to the WGCNA conventions (Bonferroni-corrected $P < 0.05$; Fig. 2a). Three of these modules are downregulated (salmon, magenta and pink) and one module is upregulated (turquoise) in Tg mice (Fig. 2a). Cell-type enrichment analysis demonstrated that the salmon module is enriched in neuronal markers, the magenta module in oligodendrocyte markers and the turquoise module in microglial, astrocyte and endothelial markers (Fig. 2b) across multiple different cell-type-specific gene expression datasets (Supplementary Fig. 4b). Gene ontology analyses are consistent with the cell-type enrichments, showing that the salmon module is enriched for synaptic pathways and magenta for DNA repair and transcription, while the turquoise module is enriched for immune and inflammatory categories (Supplementary Fig. 4c,d).

We next calculated the correlation between expression changes and an established early disease marker, the burden of hyperphosphorylated tau, which has been shown to correlate with disease progression in human FTD and AD[17,18]. Genes that correlated highly with phosphorylated (phospho)-tau levels ($R^2 > 0.6$; Methods) were found to be significantly enriched in the salmon (42-fold) and turquoise modules (9.5-fold), but not in the magenta and pink modules (Supplementary Fig. 4e) we therefore focused our subsequent analysis on the salmon and turquoise modules. Given the consistent cell-type enrichments and strong gene ontology enrichments (Fig. 2b,d–g and Supplementary Fig. 4b–d) and to provide more intuitive names for these core disease-associated modules, we relabeled the salmon module, the neurodegeneration-associated synaptic (NAS) module, and the turquoise module as the neurodegeneration-associated inflammatory (NAI) module.

To further investigate whether the expression changes were dependent on changes in cell-type composition or reflected cell-intrinsic signaling changes, we applied a multivariate linear regression model using the top 100 cell-type-specific marker genes for five major cell types[19,20] (Methods). Both modules retained their significant association with the transgenic condition (salmon, $r = -0.73$, $P = 8.6 \times 10^{-7}$; turquoise, $r = 0.71$, $P = 3 \times 10^{-6}$), indicating that they are independent of changes in cell-type composition caused by neuronal loss or gliosis. Moreover, both the NAI and NAS module eigengenes (MEs) showed changes across the affected brain regions (cortex, Fig. 2e,h; hippocampus, Supplementary Fig. 4f,g; brain stem, Supplementary Fig. 4h,i), but not the cerebellum (Fig. 2i,j), prior to decreases in brain weight that would be indicative of cell loss (Supplementary Fig. 1i). This is further supported by analysis of expression profiles from sorted neurons and glia from the Tg4510 and PS2APP AD models, which showed cell-intrinsic changes in the NAI and NAS module trajectories (Supplementary Fig. 5a–d). The NAI module was highly preserved in both microglia and astrocytes and significantly upregulated in these populations in Tg mice (Supplementary Fig. 5a,c,d–l), while the neuronal NAS module was highly preserved in sorted neurons and downregulated in Tg mice (Supplementary Fig. 5b,e–l).

We next used experimentally derived databases of human protein–protein interactions (PPI) from Inweb[21] and BioGRID[22] to create an integrated coexpression-PPI network[23] to functionally annotate network edges and provide independent validation[24] (Fig. 2c,f). One of the hubs of the NAS module, STX6, a SNARE protein[25], is also one of the few known genetic risk factors for tauopathy, having been previously implicated by genome-wide association studies (GWAS) and expression quantitative trait loci analyses in PSP. Other hub proteins, such as Syt4, Nlgn1 and Nrgn, also play important roles in synaptic maintenance and function[26,27]. Functional annotation of the NAS module with gene ontology and Kyoto Encyclopedia of Genes and Genomes terms confirms its broader relationship to synaptic function (Fig. 2d and Supplementary Fig. 4c). In contrast, functional annotation of the NAI module highlights pathways associated with astrogliosis and inflammatory changes[28], including T cell activation and Toll-like receptor signaling pathways (Fig. 2g and Supplementary Fig. 4d). Among the most central hub genes of the NAI module are *Tnip1* and *Malt1*, important inflammatory signaling genes[29]. The integrated coexpression-PPI network derived from the NAI module also contains the gene *Fus*. Mutations in this gene account for approximately 4% of familial amyotrophic lateral sclerosis (ALS), and it forms aggregates in ALS and FTD[30].

Reproducibility of disease-specific modules across mouse models and human disease. Further analysis of four independent datasets from mouse models harboring pathological tau mutations, including a replication dataset using the Tg4510 tau model (Methods and Supplementary Fig. 5f), confirms the preservation of the NAI and NAS modules (Supplementary Fig. 5e) and the expected changes in gene expression early in the disease course (Supplementary Fig. 5f–h,l). Comparison of the NAS and NAI modules in mice harboring four different AD and FTD risk mutations (PS2APP, CRND8, APP/PS1 and GRN; see Methods) was also performed to assess to what extent these modules represent convergent pathways across models harboring different pathological proteins. The NAS and NAI models are highly preserved and their disease associations are maintained; both NAI and NAS module expression changes occur with similar temporal profiles across each of these models (Supplementary Fig. 5e,i–l).

Considering this cross-mouse model conservation, we next assessed module preservation in human disease models and postmortem tissue samples to validate their human relevance (see

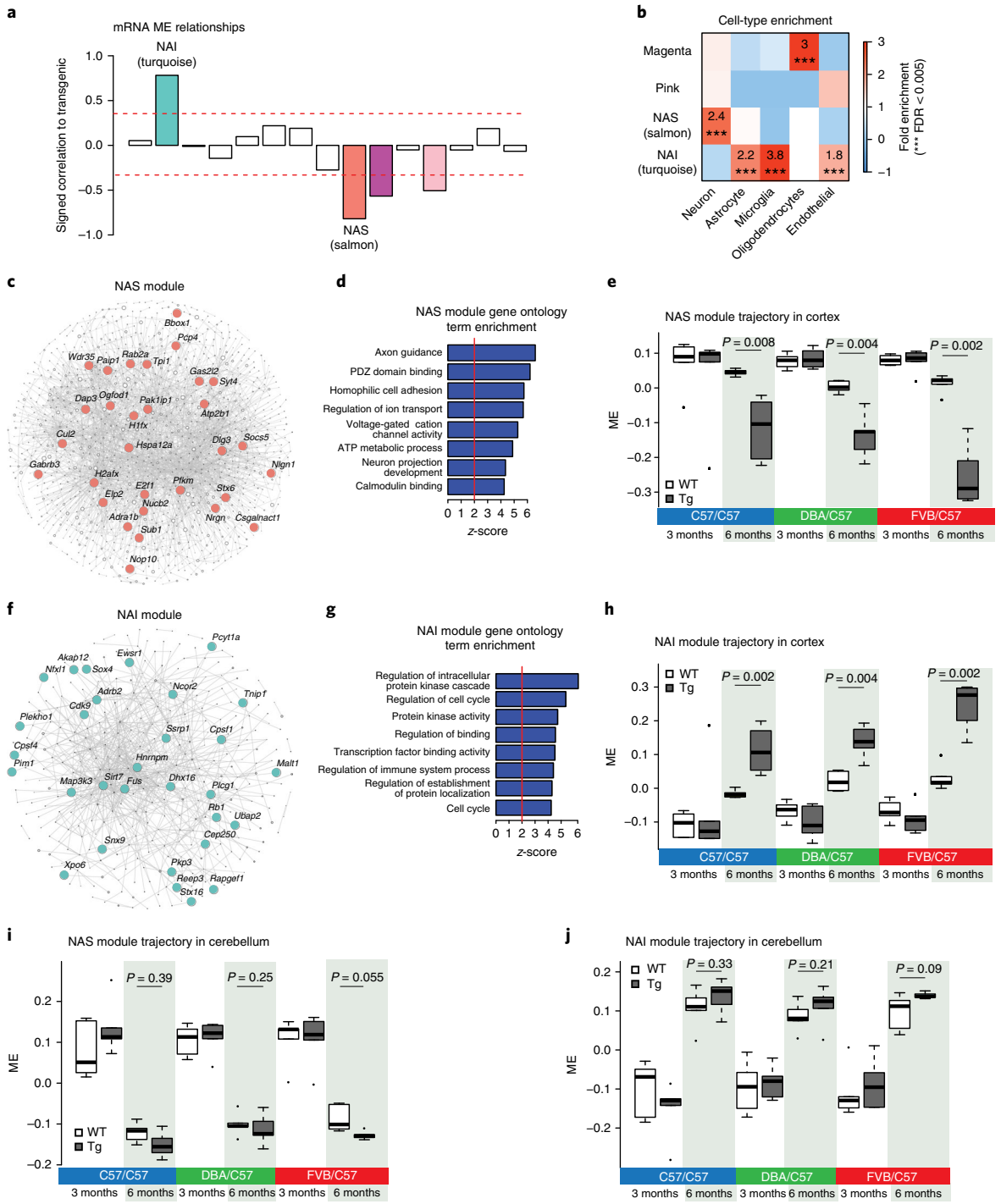

Fig. 2 | mRNA consensus coexpression network analysis. a, Signed association (Pearson correlation) of the mRNA MEs with transgenic condition. Modules with positive values indicate increased expression in transgenic mice; modules with negative values indicate decreased expression in transgenic mice. The red dotted lines indicate Bonferroni-corrected $P < 0.05$ for multiple comparisons ($n = 15$ modules, $n = 36$ mice per region) using P values obtained from two-tailed test for Pearson correlation. **b**, Cell-type enrichment of modules (average $n = 200$ genes) using mouse genes in mRNA modules (Fisher's two-tailed exact test, ***FDR < 0.005). **c**, Coexpression PPI network plot of the NAS module. The top 30 hub genes are indicated by name. The edges between nodes represent both gene coexpression and PPI, permitting us to focus on the hub genes observed at both the RNA and protein level. **d**, Gene ontology term enrichment of the NAS module using 794 NAS modules genes (permutation test z-score). **e**, Trajectory of the NAS ME in the cortex of TPR50 mice across different strains (unpaired two-sided Wilcox rank test; $n = 6$ mice per group). **f**, Coexpression PPI network plot of the NAI module. The top 30 hub genes are indicated by gene name. **g**, GO term enrichment of the NAI module using 1,833 NAI module genes. **h**, Trajectory of the NAI ME in the cortex of TPR50 mice across different strains (unpaired two-sided Wilcox rank test; $n = 6$ mice per group). **i**, Trajectory of the NAS module eigengene in the cerebellum of TPR50 mice across different strains (unpaired two-sided Wilcox rank test; $n = 6$ mice per group). **j**, Trajectory of the NAI module eigengene in the cerebellum of TPR50 mice across different strains (unpaired two-sided Wilcox rank test; $n = 6$ mice per group). In the boxplots in **e** and **h**–**j**, the upper and lower lines represent the 75th and 25th percentiles, respectively. The center line represents the median.

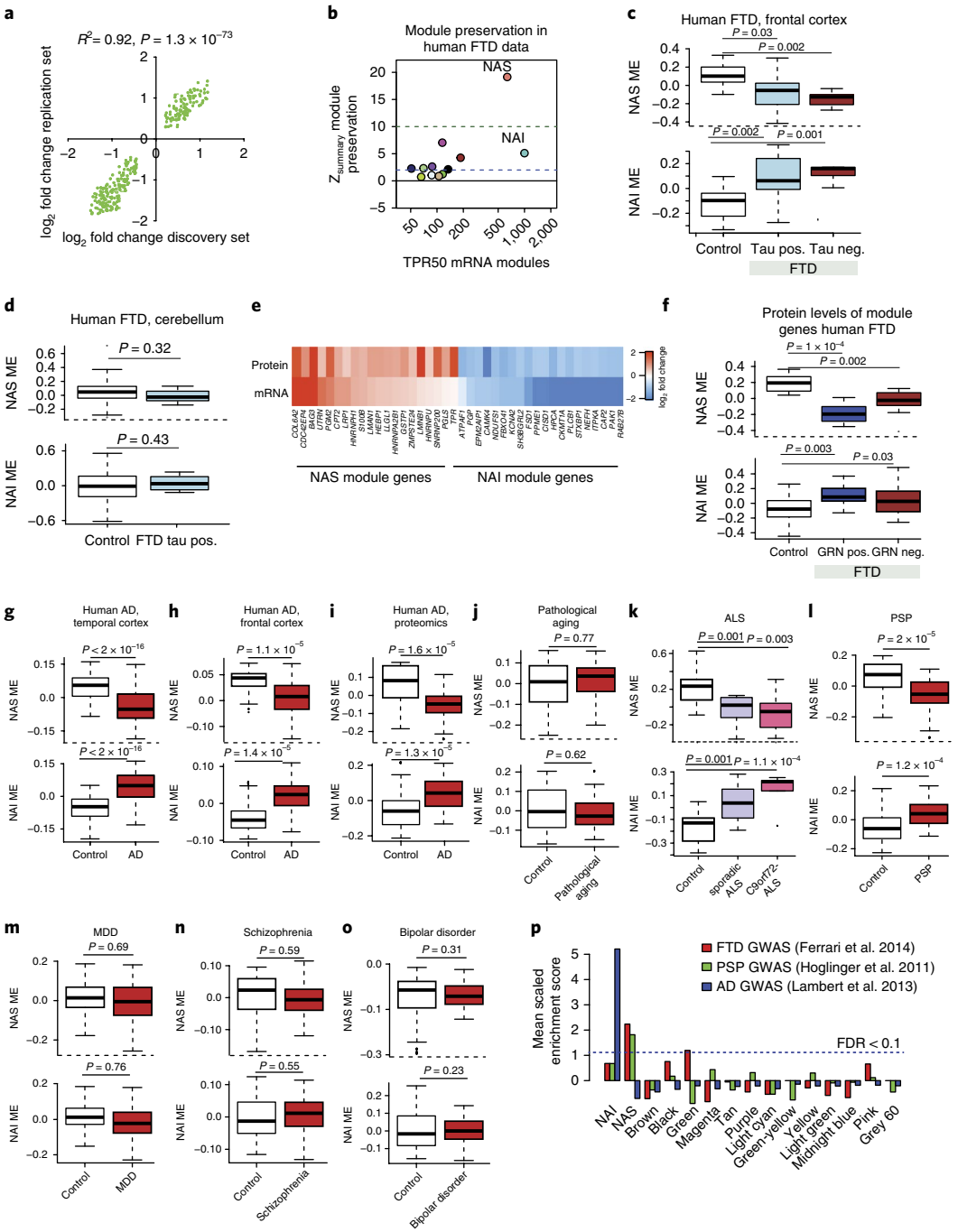

Fig. 3 | Transcriptomic and proteomic analyses in human FTD samples. a, Scatterplot showing Pearson correlation of subsampled discovery (control $n=7$, tau-positive FTD $n=5$) and replication FTD (control $n=7$, tau-positive FTD $n=5$) datasets. The *P* values obtained from two-sided tests for Pearson correlation are shown. **b**, Module preservation in human FTD (cortex) using module definitions from strain-independent transgenic mouse network analysis. **c**,**d**, NAS and NAI ME expression in human FTD and control samples in the cortex (**c**, control $n=14$, tau-positive FTD $n=10$, tau-negative FTD $n=6$) and cerebellum (**d**, control $n=10$, tau-positive FTD $n=7$). Tau-positive FTD (FTD-tau pos.) and tau-negative FTD (FTD-tau neg.) are shown (unpaired two-sample Wilcoxon rank-sum test). **e**, $\log_2$ fold change of the top 20 NAS and NAI module genes at the mRNA and protein level. **f**, NAS and NAI ME in human FTD and control protein samples from the cortex. GRN-positive FTD (FTD GRN pos.) and GRN-negative FTD (FTD GRN neg.) are shown (unpaired two-sample Wilcoxon rank-sum test; control $n=8$, GRN-Pos. $n=6$, GRN-Neg. $n=10$). **g**–**o**, NAS and NAI MEs in various neurological diseases: human AD temporal cortex (**g**, control $n=52$, AD $n=52$)[44]; human AD frontal cortex (**h**, control $n=308$, AD $n=157$)[36]; human AD frontal cortex proteomics (**i**, control $n=15$, AD $n=20$)[45]; human pathological aging temporal cortex (**j**, control $n=70$, pathological aging $n=30$)[44]; human ALS frontal cortex (**k**, control $n=9$, C9orf ALS $n=8$, Sporadic ALS $n=10$)[46]; human PSP temporal cortex (**l**, control $n=73$, PSP $n=83$)[44]; human major depressive disorder (MDD) (**m**, control $n=67$, MDD $n=66$)[47]; human schizophrenia (**n**, control $n=167$, schizophrenia $n=131$)[48]; and bipolar disorder (**o**, control $n=65$, bipolar disorder $n=40$)[48]. Unpaired two-sample Wilcoxon rank-sum test. In all the boxplots, the upper and lower lines represent the 75th and 25th percentiles, respectively. The center line represents the median. **p**, Mean scaled enrichment of GWAS hits (calculated *P* value < 0.05) from FTD GWAS[49], PSP GWAS[50] and AD GWAS[51] in various TPR50 modules ($n=15$ modules). NAI module enrichment for AD risk genes was still significant after omitting *APOE* from the analysis (Supplementary Table 4d).

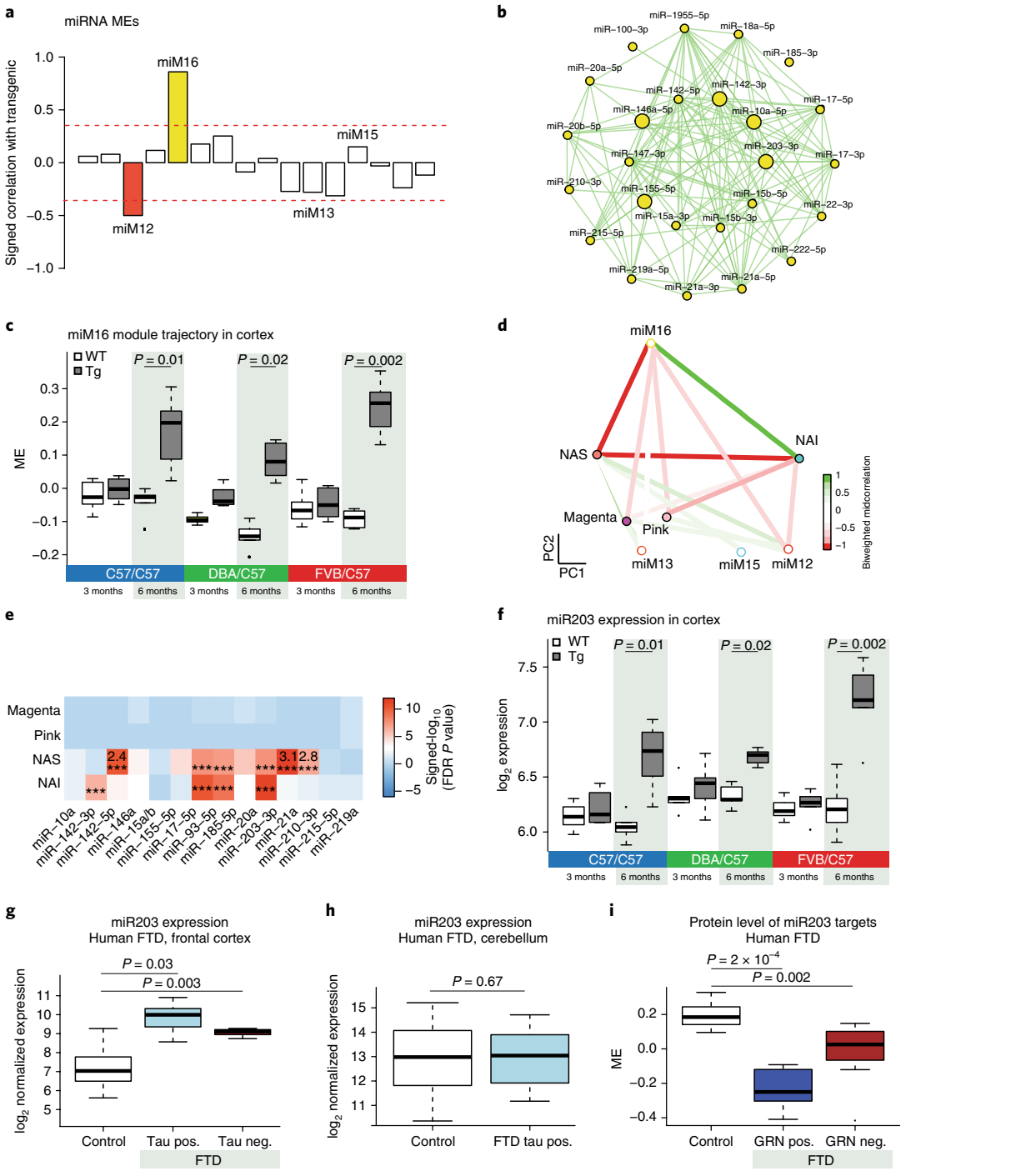

Fig. 4 | miRNA coexpression network analysis. a, Signed association (Pearson correlation) of the miRNA MEs with transgenic condition. Modules with positive values indicate increased expression in transgenic mice; modules with negative values indicate decreased expression in transgenic mice. The red dotted lines indicate Bonferroni-corrected $P < 0.05$ for multiple comparisons ($n = 16$ modules) using P values obtained from a two-sided test for Pearson correlation. **b**, miRNA coexpression network plot of the miM16 module showing hub miRNAs in the center. Large nodes indicate the top five hub miRNAs. **c**, Trajectory of the miM16 module in the cortex (unpaired two-sample Wilcoxon rank-sum test, $n = 6$ mice per group). **d**, Multidimensional scaling plot illustrating the correlations between the MEs of the mRNA and miRNA modules. The colors indicate biweighted midcorrelation (R) values. **e**, Enrichment of selected miM16 module miRNA predicted targets in the mRNA modules. All enrichment values (odds ratio (OR)) with FDR < 0.05 and OR > 2 are shown (Fisher's two-sided exact test, ***FDR < 0.005). For a full list of enrichments, refer to Supplementary Fig. 6g. The TargetScan database was used for miRNA target prediction. **f**, Trajectory of $\log_2$ expression of miR-203 in the cortex (unpaired two-sample Wilcoxon rank-sum test; $n = 6$ mice per group). **g**,**h**, miR-203 expression in the cortex (**g**, control $n = 14$, tau-positive FTD $n = 10$, tau-negative FTD $n = 6$) and cerebellum (**h**, control $n = 10$, tau-positive FTD $n = 7$) of human FTD and control samples. Tau-positive FTD (FTD-tau pos.) and tau-negative FTD (FTD-tau neg.) are shown for the cortex (unpaired two-sample Wilcoxon rank-sum test). **i**, ME of predicted targets of miR-203 expression in human FTD and control protein samples in the cortex. Control $n = 8$, FTD GRN pos. $n = 6$, FTD GRN neg. $n = 10$, GRN-positive FTD (FTD GRN pos.) and progranulin-negative FTD (FTD GRN neg.) are shown (unpaired two-sample Wilcoxon rank-sum test). In all the boxplots, the upper and lower lines represent the 75th and 25th percentiles, respectively, while the center line represents the median.

Methods, Supplementary Table 2a for list and characteristics of all human datasets, and Supplementary Table 2b,c). The NAS and NAI modules are dysregulated in the cortex of patients, but not in the cerebellum, both in previously published microarray-based data and in our newly generated RNA-seq dataset (Fig. 3a–d and Supplementary Fig. 5e,m,n) consisting of both tau-positive and tau-negative FTD (Fig. 3c). Moreover, the NAS module and its disease–trait relationship are preserved in induced pluripotent stem cell (iPSC)-derived neurons from human FTD patients carrying GRN mutations (Supplementary Fig. 5e,o).

We also performed mass spectrometry–based, label-free, quantitative proteomics in an independent set of GRN-positive and GRN-negative FTD frontal cortex samples (Supplementary Fig. 5p, Supplementary Table 2d and Methods). We found similar NAI and NAS expression patterns at the mRNA and protein level (Fig. 3e) both in GRN-positive and GRN-negative FTD samples, compared with age-matched controls (Fig. 3f). Taken together, our analyses show that the NAS and NAI coexpression modules are conserved across multiple model systems and generalize from mouse to human, reflecting convergent RNA coexpression and protein-level changes in FTD.

Examination of RNA-seq and proteomic postmortem brain dataset from patients with AD showed preservation of both the NAI and the NAS modules at the mRNA (Fig. 3g,h, Supplementary Fig. 5e and Supplementary Table 4a) and protein (Fig. 3i) level. Notably, both modules are not dysregulated in cases of pathological aging without dementia ($P=0.77$; Fig. 3j), indicating that they are not related to the presence of Aβ amyloid plaques alone[31]. The NAS and NAI modules are also dysregulated in C9orf72-related and sporadic ALS (Fig. 3k) and PSP (Fig. 3l), but not in major depression (Fig. 3m), schizophrenia (Fig. 3n) or bipolar disorder (Fig. 3o). These results support the relevance and specificity of these changes to allied human neurodegenerative syndromes, but not other nondegenerative forms of neuropsychiatric disorders.

Assessment of genetic risk within modules. Transcriptomic changes may be the cause or consequence of disease, so integrating these data with genetic risk data provides a means to further understand their relationship to potential causal mechanisms (for example, see refs [32,33]). Several AD candidate genes, including *APOE, CLU, PICALM, C1q* and *TREM2* mapped to the NAI module (Fig. 3p, Methods and Supplementary Table 1i); in contrast to AD, FTD and PSP, GWAS data showed significant enrichment in the NAS module, which contains risk genes such as *SLC32A1*, *NSF* and *ELAVL2* (Fig. 3p). These differential module enrichments indicate that the genetic risk for AD, FTD and PSP likely operates via distinct causal pathways that may converge on common downstream neuronal and glial-immune processes.

Identification of potential miRNA drivers. Based on the strong co-expression relationships observed in the NAS and NAI modules, we hypothesized potential coregulation by miRNA. We identified two miRNA modules associated with the transgenic condition (Bonferroni-corrected $P<0.05$; Fig. 4a and Supplementary Table 3): the miM12 module, which is anticorrelated, and the miM16 module (Fig. 4b), which is positively correlated with the transgenic condition in affected regions, but not the cerebellum (Fig. 4c and Supplementary Fig. 6a–e). The miM16 ME is strongly anticorrelated with the NAS ME (Fig. 4d and Supplementary Fig. 6f), and predicted targets of miR-203, an miM16 hub, are highly enriched (Methods) in the NAS module (Fig. 4e and Supplementary Fig. 6g,h). Consistent with its potential regulatory role, miR-203 is robustly upregulated in Tg mice at 6 months in disease-affected areas (Fig. 4f and Supplementary Fig. 6i–k) and in the frontal cortex in both tau-positive and tau-negative FTD (Fig. 4g,h). Protein levels of its targets are also significantly decreased in both granulin-positive and granulin-negative FTD ($P<0.005$; Fig. 4i). These data across mouse and humans suggested that miR-203 may be acting as a driver of the NAS neurodegeneration-associated transcriptional program.

Fig. 5 | Overexpression of miR-203 in vitro and in vivo. **a**, Schematic of the lentiviral vector used for the in vitro studies. **b**,**c**, Trajectory of the miR-203 target genes (**b**) and NAS ME (**c**) in uninfected primary cortical cultures or cultures infected with either miR-203- or sc-miRNA-lentiviral construct (unpaired two-sample Wilcoxon rank-sum test; $n=4$ per group). **d**, Representative images of TUNEL staining from three independent experiments in mouse primary cortical neurons overexpressing miR-203 or sc-miRNA (control) at DIV6, DIV8 and DIV10 days. Green, GFP (infection); red, TUNEL; blue, Hoechst. Scale bar, 25 µm. **e**, Quantification of TUNEL staining. The percentage of TUNEL-positive cells in miR-203-overexpressing cultures were normalized at each time point to the average percent of TUNEL-positive cells in the sc-miRNA control (unpaired two-tailed *t*-test; $n=60$ cells for DIV6, $n=50$ for DIV8 and $n=60$ cells for DIV10). The center line represents the mean, and error bars show s.e.m. **f**, Normalized luminescence of luciferase reporter assay. Luciferase vectors containing 950 bp of the 3′-UTR sequence of the *Bcl2l2*, *Dgkb*, *Mapk10*, *Vsnl1* and *Npepps* genes were cotransfected with 20 nM miR-203 or control mimics in HEK 293T cells and assayed after 24–48 h (unpaired two-tailed *t*-test; $n=12$ per group). The center line represents the mean, and error bars show s.e.m. **g**, Representative immunoblots from three independent experiments and quantification of BCL2L2 and VSNL1 protein levels from total cell lysates isolated from primary mouse cortical neurons overexpressing miR-203 or sc-miRNA (paired two-tailed *t*-test). The center line represents the mean, and error bars show s.e.m. Uncropped blots are shown in Supplementary Fig. 9. **h**, Schematic representation of experimental design and timeline to overexpress or inhibit miR-203 in C57BL/6 WT or Tg4510 tau transgenic mouse frontal cortex using the AAV2/9 system. **i**, NAS ME expression in GFP-positive cells overexpressing miR-203 or sc-miRNA at 3 or 6 weeks after AAV injection in C57BL/6 WT mice (unpaired two-sample Wilcoxon rank-sum test; $n=6$ per group). **j**, Expression of genes involved in positive (GO:0043065) and negative (GO:0043066) regulation of apoptosis in GFP-positive cells overexpressing miR-203 or sc-miRNA at 3 and 6 weeks after AAV injection in C57BL/6 WT mice (unpaired two-sample Wilcoxon rank-sum test; $n=6$ per group). **k**, The CASP-8 intensity of GFP-positive cells overexpressing miR-203 were normalized at each time point to the average CASP-8 intensity of GFP-positive cells overexpressing sc-miRNA control (unpaired two-tailed Mann–Whitney *U*-test; $n=464$ cells for the 3-weeks control, $n=937$ cells for the 3-weeks miR-203, $n=629$ cells for the 6-weeks control, $n=1{,}441$ cells for the 6-weeks miR-203; three independent biological replicates per condition). The center line represents the mean, the error bars show the s.e.m. **l**,**m**, ME of miR-203 targets (**l**) or NAS module (**m**) in GFP-positive cells overexpressing miR-203 6 weeks after AAV injection (unpaired two-sample Wilcoxon rank-sum test; $n=5$ sc-miRNA-infected mice and $n=6$ miR203-infected mice). **n**, The CASP-8 intensity of GFP-positive cells overexpressing miR-203 in Tg4510 tau transgenic mice was normalized at each time point to the average CASP-8 intensity of GFP-positive cells overexpressing the sc-miRNA control (unpaired two-tailed Mann–Whitney *U*-test; $n=507$ cells for sc-miRNA and 2,793 cells for miR-203, 3 independent biological replicates per condition). The center line represents the mean, and the error bars show the s.e.m. **o**,**p**, ME of miR-203 targets (**o**) or NAS module (**p**) in GFP-positive cells overexpressing the sc-TuD control or miR-203 TuD 6 weeks after AAV injection in Tg4510 tau Tg mice (unpaired two-sample Wilcoxon rank-sum test; $n=5$ sc-miRNA infected mice and $n=6$ miR203 infected mice). In all the boxplots, the upper and lower lines represent the 75th and 25th percentiles, respectively, while the center line represents the median. **q**, The c-Fos intensity of GFP-positive cells expressing TuD-miR203 in Tg4510 tau transgenic mice was normalized at each time point to the average c-Fos intensity of GFP-positive cells expressing the sc-TuD control (unpaired two-tailed *t*-test; $n=50$ images (control) and $n=60$ images (miR203), $n=5$ sc-miRNA-infected mice and $n=6$ miR203-infected mice). The center line represents the mean, and the error bars show the s.e.m.

miR-203 regulates the neuronal mRNA module and causes cell death. To test the predicted causal relationship between miR-203 expression and NAS module downregulation, we acutely overexpressed miR-203 (Fig. 5a) in primary cortical mouse neuronal cultures (Methods and Supplementary Fig. 7a), observing downregulation of its predicted targets (Fig. 5b) and the NAS module more broadly (Fig. 5c, Supplementary Fig. 7b and Supplementary Table 4a). We also observed increased apoptosis (Fig. 5d), peaking at DIV8 (1.85-fold; Fig. 5e), concurrent with peak NAS module downregulation. We further experimentally validated several predicted direct targets of miR-203 (*Bcl2l2*, *Dgkb*, *Mapk10*, *Vsnl1*) by luciferase reporter assays (Fig. 5f) and western blot (BCL2L2 and VSNL1; Fig. 5g, see Supplementary Fig. 9 for uncropped blots).

To control for potential confounding by supraphysiological overexpression in vitro, we moderately overexpressed miR-203 (approximately twofold; Methods) or a scrambled miRNA control (sc-miRNA) (Fig. 5h) targeting neurons in WT mice in vivo (Supplementary Fig. 7c–f). The NAS module is highly preserved (Supplementary Fig. 7g and Supplementary Table 4a) and downregulated in neurons overexpressing miR-203 after 6 weeks (Fig. 5i). Strikingly, the level of miR-203 expression correlates remarkably well with the downregulation of both miR-203 predicted targets ($R^2 = 0.81$, slope = −2.3; Supplementary Fig. 7h) and NAS module genes ($R^2 = 0.81$, slope = −2.2; Supplementary Fig. 7i). Furthermore, apoptotic pathways are altered in miR-203-overexpressing neurons (Fig. 5j and Supplementary Table 4b), confirmed by caspase-8

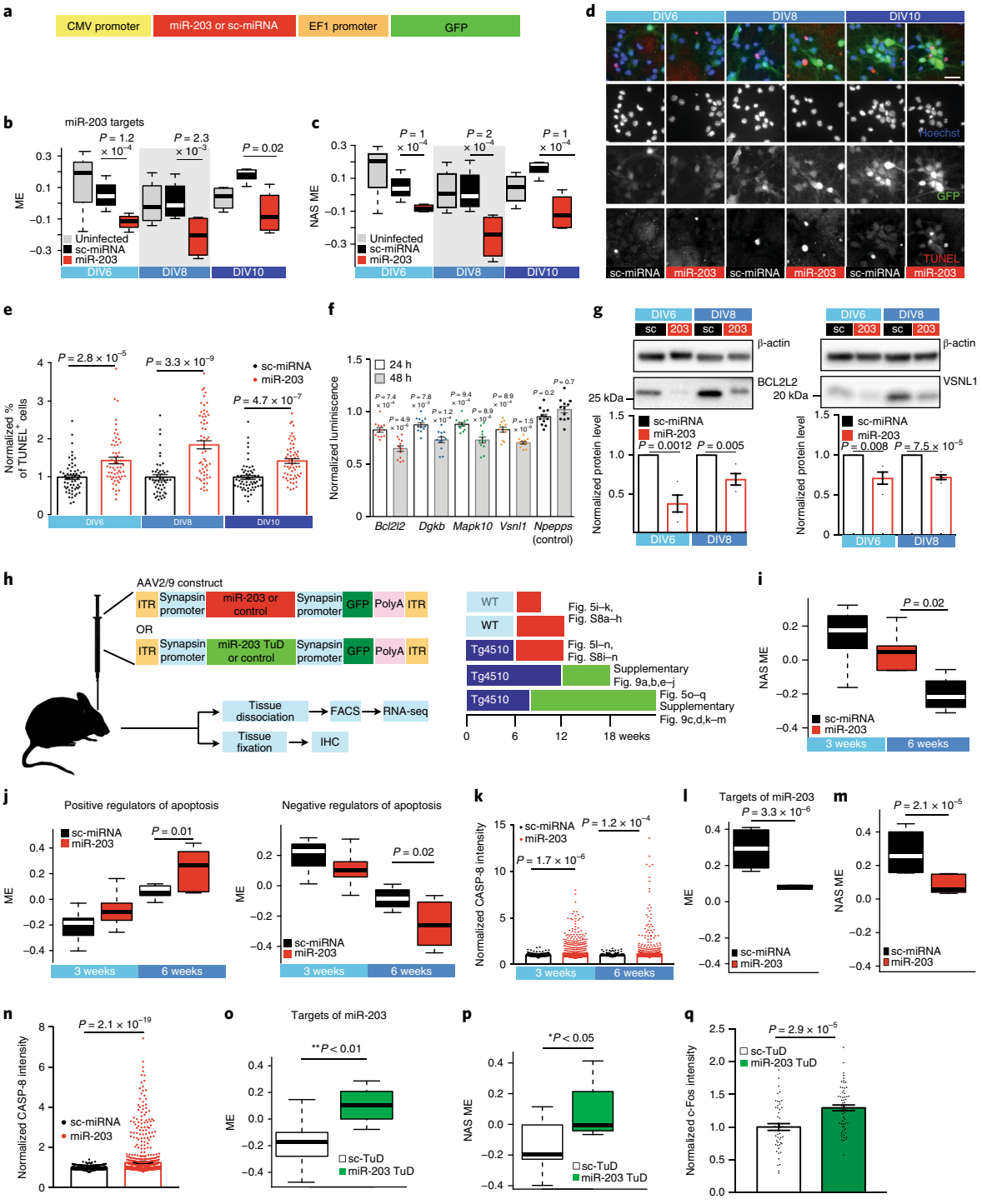

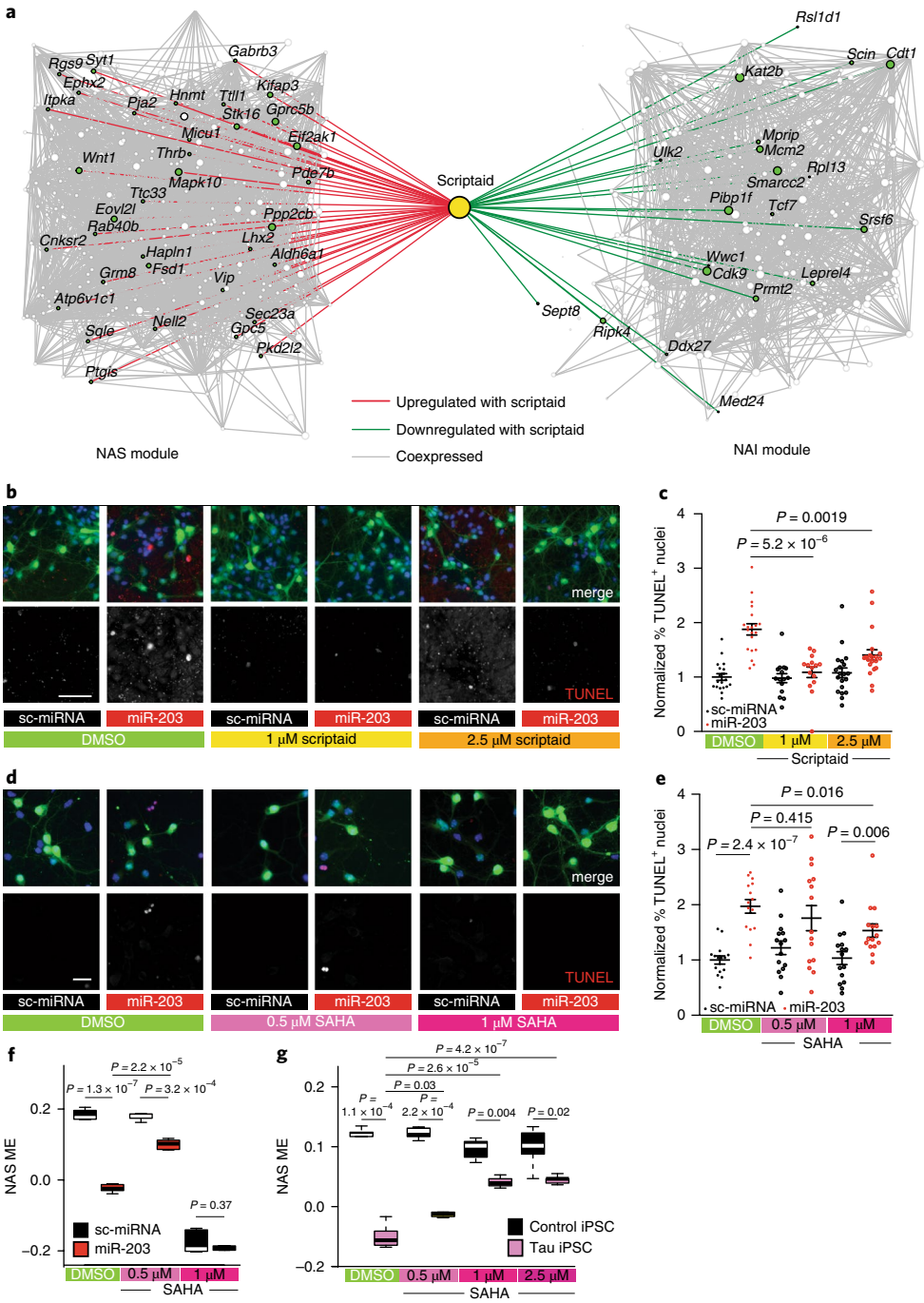

Fig. 6 | Small-molecule inhibition of miR-203-induced cell death in vitro. a, Coexpression-based network plot of scriptaid targets from the CMAP database with genes in the NAS and NAI modules. Genes that are upregulated with scriptaid treatment are connected by red edges; those that are downregulated are connected by green edges. Node size represents centrality within the network. **b**, Representative images from three independent experiments of TUNEL staining in mouse primary cortical neurons overexpressing miR-203 or sc-miRNA (control) at DIV7 treated with DMSO control and 1 μM or 2.5 μM scriptaid or DMSO control for 24 h prior. Green, GFP; red, TUNEL; blue, Hoechst. Scale bar, 25 mm. **c**, Quantification of TUNEL-positive cells treated with scriptaid in three independent experiments (unpaired two-tailed *t*-test; $n = 20$ per group). Scriptaid treatment does not alter miR-203 overexpression levels (Supplementary Fig. 9), indicating that the decrease in cell death is not a result of changes in viral infection, miRNA processing or regulation of miR-203 by scriptaid. The center line represents the mean, and error bars show s.e.m. **d**, Representative images from three independent experiments of TUNEL staining in mouse primary cortical neurons overexpressing miR-203 or sc-miRNA (control) at DIV7 treated with DMSO control and 0.5 μM or 1 μM SAHA for 24 h prior. Green, GFP; red, TUNEL; blue, Hoechst. Scale bar, 25 mm. **e**, Quantification of TUNEL positive cells from three independent experiments treated with SAHA (unpaired two-tailed *t*-test; $n = 15$ per group). The center line represents the mean and error bars showing s.e.m. **f**, Trajectory of the NAS ME in cultures infected with either the miR-203- or sc-miRNA-lentiviral construct treated with either DMSO control or 0.5 μM or 1 μM SAHA (unpaired two-tailed Wilcox rank test; $n = 6$ per group). **g**, Trajectory of the NAS ME in human iPSC-derived neurons from control and A152T Tau patients treated with either DMSO control or 0.5 μM, 1 μM or 2.5 μM SAHA (unpaired two-tailed Wilcox rank test; $n = 6$ per group). In all the boxplots, the upper and lower lines represent the 75th and 25th percentiles, respectively, while the center line represents the median.

(CASP-8) protein expression (Fig. 5k and Supplementary Fig. 7j). Additionally, miR-203 overexpression in 1-month-old Tg4510 tau transgenic cortex (Supplementary Fig. 8a,b) causes downregulation of predicted miR-203 targets (Fig. 5l), the NAS module (Fig. 5m), genes involved in calcium signaling and neuroactive ligand receptors (Supplementary Fig. 8e,f) and a significant increase in CASP-8 protein (Fig. 5n) and apoptotic pathways (Supplementary Fig. 8c,d).

To further investigate the causal role of miR-203, we inhibited miR-203 expression in neurons using a 'Tough Decoy' (TuD) adeno-associated virus (AAV) system[34] in vivo in Tg4510 mice (Fig. 5h). Both short-term (6 weeks; Supplementary Fig. 8g,h) and longer-term (4 months; Supplementary Fig. 8i,j) inhibition of miR-203 oppose the pathological transcriptional changes in predicted miR-203 targets (Fig. 5o and Supplementary Fig. 8k) and the NAS module broadly (Fig. 5p and Supplementary Fig. 8l), including genes involved in calcium signaling and neuroactive ligand receptor pathways (Supplementary Fig. 8m,n), and apoptosis (Fig. 5q and Supplementary Fig. 8o,p). Reducing miR-203 did not affect phospho-tau immunostaining (Supplementary Fig. 8q,r), which is consistent with its acting downstream of tau pathology. Previous work has shown that 5-month-old Tg4510 mice show reduced neocortical network activity based on proto-oncogene c-Fos immunoreactivity[35]. C-Fos intensity was also significantly increased in mutant neurons expressing the miR-203 TuD construct, compared to those expressing the control construct ($P<0.0001$; Fig. 5q and Supplementary Fig. 8s), suggesting functional rescue. These findings demonstrate that inhibition of miR-203 can reverse the expression patterns of both the NAS module and apoptotic pathway genes associated with disease state in vivo, while overexpression of miR-203 promotes downregulation of the NAS module and a neurodegenerative phenotype.

Pharmacological manipulation of NAS module genes. We reasoned that if the patterns of gene expression robustly associated with disease state across mice and humans represented causal phenomena, as suggested by GWAS enrichment, then their reversal should ameliorate the miR-203-mediated cell death phenotype. To test this, we screened the Connectivity Map (CMAP), a public compendium of cell line gene expression responses to drugs, to identify small molecules predicted to reverse the NAS or NAI module changes observed across pathological conditions, albeit in nonneuronal cells. Four of the top ten hits were histone deacetylase inhibitors (Supplementary Table 4c), which was significant (permutated $P<1\times10^{-5}$).

We chose two of the predicted molecules, scriptaid, which was the top hit in CMAP (enrichment score = −0.969; Fig. 6a) and suberanilohydroxamic acid (SAHA) (vorinostat; enrichment score = −0.846), which is undergoing human clinical trials (NCT03056495). As predicted, adding scriptaid to miR-203-overexpressing neurons decreased the neuronal death caused by miR-203 overexpression to levels equivalent to controls (unpaired *t*-test; Fig. 6b,c). We also found that 0.5 µM SAHA decreased miR-203-induced cell death (Fig. 6d,e). SAHA upregulated NAS module genes (Fig. 6f); however, SAHA showed toxicity at 1 µM even in control neurons (Fig. 6f). Next, we treated human iPSC-derived neurons from controls and patients with FTD with SAHA, observing that SAHA upregulates NAS module genes in a dose-dependent manner (Fig. 6g). Therefore, we conclude that miR-203 directly regulates many NAS module hub genes and that the histone deacetylase inhibitors, scriptaid and SAHA, by targeting the NAS and NAI module genes and normalizing their expression, can ameliorate miR-203-induced proneurodegenerative changes.

Discussion

The mechanisms underlying neurodegenerative diseases are still poorly understood, a factor that impedes the design of therapeutic interventions to treat these disorders. Rather than focusing on a priori candidate genes, we pursued a systematic, genome-wide, functional genomics approach. Such studies have not been realized in the study of most neurodegenerative diseases, with a few notable exceptions[36–38]. By taking genetic background into consideration, representing diverse causal mutations in transcriptomic network analyses and validation in a dozen independent datasets, we identify disease-relevant gene networks representing specific molecular pathways. It is noteworthy that modules identified in the initial individual F1 crosses that are not conserved and dysregulated across all three strains are also not conserved in other mouse models or the human brain (Supplementary Fig. 10a–c), supporting the approach we have taken.

In functional genomic studies, each experimental system on its own, whether in vitro systems, in vivo mouse models or postmortem human tissue, has significant limitations[39]. In this study, we show how a multistage systems biology analysis coupled with substantial in vitro experimental validation provides a framework for discovery of new disease mechanisms and therapeutic targets. We leverage the benefits of animal models of human disease, which permit the temporal assessment of changes before substantial atrophy and cell loss while mitigating the potential bias introduced by a single genetic background. We also consider the principles of regional vulnerability and disease trajectories[12,40] and find that gene networks associated with transgenic status are altered in brain areas that show signs of neurodegeneration. Conversely, in the cerebellum, a brain region that is spared in AD and FTD, the expression of the NAS and NAI modules, as well as miR-203, does not change significantly.

A key issue in any analysis of gene expression in disease is that changes in gene expression may be either a cause or consequence of the disorder. To advance our work toward identifying causal drivers, we experimentally validate a putative miRNA driver of the altered transcriptional networks, miR-203, which has previously not been implicated in neurodegeneration, and we show reversal by gene-network-predicted pharmacological regulators. We also find significant enrichment of common genetic risk for both FTD and PSP in the neuronal NAS module and enrichment for AD GWAS signals in the NAI module, which is enriched in glial and immune genes. These data further support the potential causal role of these modules and suggest different causal pathways in AD versus FTD and PSP, the latter of which are considered primary tauopathies[3,4]

It is important to note that both expression changes in the disease-associated gene modules NAS and NAI, as well as the upregulation of miR-203, though clearly a point of convergence, are most likely downstream of initial pathological insults, whether caused by tau or other major risk genes. From this perspective, these modules represent robust, highly conserved biological processes that provide a crucial link in the chain between an initial causal genetic insult and neuronal death and inflammation. As we show, long-term inhibition of miR-203 in the Tg4510 model, while upregulating antiapoptotic pathways, downregulating proapoptotic pathways and increasing neuronal activity as measured by c-Fos activation, does not reduce the phospho-tau burden (Supplementary Fig. 8q,r). Though pharmacologically targeting these gene networks, or miR-203 itself, may not reverse tau aggregation or Aβ plaque formation, it may provide a means to uncouple dysfunction of aggregation-prone proteins from inflammation, neurodegeneration and their behavioral outcome—dementia. Supporting this possibility is the fact that neither the NAS nor the NAI modules are dysregulated in patients that show pathological aging, in which significant amyloid plaque density, but no dementia, is observed. Therefore, developing therapies that reverse the changes in the disease-associated gene coexpression modules may be an opportunity to impede neurodegeneration across a broad spectrum of dementias without having to target unique upstream pathological events. Moreover, we hypothesize that regulators of these highly conserved transcriptional programs, such as miR-203, may be new therapeutic targets.

Efforts to target miRNAs to treat diseases are already underway[41] and traditional antisense oligo-based targets have reached clinical trials[42], while small-molecule modulators represent a new frontier in miRNA-based therapeutics[43]. In this regard, identifying regulators of the NAI module is also likely to be a fertile avenue for future studies aimed at therapeutic development[44].

URLs. miRbase, http://www.mirbase.org/; TargetScan database, http://www.targetscan.org/vert_72/; CMP database, https://portals.broadinstitute.org/cmap/.

Online content

Any methods, additional references, Nature Research reporting summaries, source data, statements of data availability and associated accession codes are available at https://doi.org/10.1038/s41591-018-0223-3.

Received: 20 November 2017; Accepted: 18 September 2018;
Published online: 03 December 2018

References

1. Hinz, F. I. & Geschwind, D. H. Molecular genetics of neurodegenerative dementias. *Cold Spring Harb. Perspect. Biol.* **9**, a023705 (2017).
2. Iqbal, K., Liu, F. & Gong, C. X. Tau and neurodegenerative disease: the story so far. *Nat. Rev. Neurol.* **12**, 15–27 (2016).
3. Masters, C. L. et al. Alzheimer's disease. *Nat. Rev. Dis. Primers* **1**, 15056 (2015).
4. Kovacs, G. G. Invited review: neuropathology of tauopathies: principles and practice. *Neuropathol. Appl. Neurobiol.* **41**, 3–23 (2015).
5. Mullane, K. & Williams, M. Alzheimer's therapeutics: continued clinical failures question the validity of the amyloid hypothesis—but what lies beyond? *Biochem. Pharmacol.* **85**, 289–305 (2013).
6. Institute of Medicine. *Improving the Utility and Translation of Animal Models for Nervous System Disorders: Workshop Summary* (The National Academies Press, Washington DC, 2013).
7. Miller, J. A., Horvath, S. & Geschwind, D. H. Divergence of human and mouse brain transcriptome highlights Alzheimer disease pathways. *Proc. Natl. Acad. Sci. USA* **107**, 12698–12703 (2010).
8. Qosa, H. & Kaddoumi, A. Effect of mouse strain as a background for Alzheimer's disease models on the clearance of amyloid-β. *J. Syst. Integr. Neurosci.* **2**, 135–140 (2016).
9. Weitzner, D. S., Engler-Chiurazzi, E. B., Kotilinek, L. A., Ashe, K. H. & Reed, M. N. Morris Water Maze Test: optimization for mouse strain and testing environment. *J. Vis. Exp.* e52706 (2015).
10. LaFerla, F. M. & Green, K. N. Animal models of Alzheimer disease. *Cold Spring Harb. Perspect. Med.* **2**, a0066320 (2012).
11. Webster, S. J., Bachstetter, A. D., Nelson, P. T., Schmitt, F. A. & Van Eldik, L. J. Using mice to model Alzheimer's dementia: an overview of the clinical disease and the preclinical behavioral changes in 10 mouse models. *Front. Genet.* **5**, 88 (2014).
12. Karsten, S. L. et al. A genomic screen for modifiers of tauopathy identifies puromycin-sensitive aminopeptidase as an inhibitor of tau-induced neurodegeneration. *Neuron* **51**, 549–560 (2006).
13. Onishi, T. et al. Early-onset cognitive deficits and axonal transport dysfunction in P301S mutant tau transgenic mice. *Neurosci. Res.* **80**, 76–85 (2014).
14. Yoshiyama, Y. et al. Synapse loss and microglial activation precede tangles in a P301S tauopathy mouse model. *Neuron* **53**, 337–351 (2007).
15. Zhang, B. & Horvath, S. A general framework for weighted gene co-expression network analysis. *Stat. Appl. Genet. Mol. Biol.* **4**, Article17 (2005).
16. Langfelder, P. & Horvath, S. WGCNA: an R package for weighted correlation network analysis. *BMC Bioinformatics* **9**, 559 (2008).
17. Spillantini, M. G. & Goedert, M. Tau protein pathology in neurodegenerative diseases. *Trends Neurosci.* **21**, 428–433 (1998).
18. Braak, H. & Braak, E. Neuropathological stageing of Alzheimer-related changes. *Acta Neuropathol.* **82**, 239–259 (1991).
19. Kuhn, A., Thu, D., Waldvogel, H. J., Faull, R. L. M. & Luthi-Carter, R. Population-specific expression analysis (PSEA) reveals molecular changes in diseased brain. *Nat. Methods* **8**, 945–947 (2011).
20. Miller, J. A., Woltjer, R. L., Goodenbour, J. M., Horvath, S. & Geschwind, D. H. Genes and pathways underlying regional and cell type changes in Alzheimer's disease. *Genome Med.* **5**, 48 (2013).
21. Lage, K. et al. A human phenome–interactome network of protein complexes implicated in geneticdisorders.*Nat. Biotechnol.* **25**, 309–316 (2007).
22. Stark, C. et al. BioGRID: a general repository for interaction datasets. *Nucleic Acids Res.* **34**, D535–D539 (2006).
23. Parikshak, N. N. et al. Integrative functional genomic analyses implicate specific molecular pathways and circuits in autism. *Cell* **155**, 1008–1021 (2013).
24. Parikshak, N. N., Gandal, M. J. & Geschwind, D. H. Systems biology and gene networks in neurodevelopmental and neurodegenerative disorders. *Nat. Rev. Genet.* **16**, 441–458 (2015).
25. Murray, R. Z., Wylie, F. G., Khromykh, T., Hume, D. A. & Stow, J. L. Syntaxin 6 and Vti1b form a novel SNARE complex, which is up-regulated in activated macrophages to facilitate exocytosis of tumor necrosis Factor-alpha. *J. Biol. Chem.* **280**, 10478–10483 (2005).
26. Gjørlund, M. D. et al. Neuroligin-1 induces neurite outgrowth through interaction with neurexin-1β and activation of fibroblast growth factor receptor-1. *FASEB J.* **26**, 4174–4186 (2012).
27. Huang, K. P. et al. Neurogranin/RC3 enhances long-term potentiation and learning by promoting calcium-mediated signaling. *J. Neurosci.* **24**, 10660–10669 (2004).
28. Jaworski, M. et al. Malt1 protease inactivation efficiently dampens immune responses but causes spontaneous autoimmunity. *EMBO J.* **33**, 2765–2781 (2014).
29. Lessard, C. J. et al. Variants at multiple loci implicated in both innate and adaptive immune responses are associated with Sjögren's syndrome. *Nat. Genet.* **45**, 1284–1292 (2013).
30. Ng, A. S. L., Rademakers, R. & Miller, B. L. Frontotemporal dementia: a bridge between dementia and neuromuscular disease. *Ann. N. Y. Acad. Sci.* **1338**, 71–93 (2015).
31. Maeda, S. et al. Expression of A152T human tau causes age-dependent neuronal dysfunction and loss in transgenic mice. *EMBO Rep.* **17**, 530–551 (2016).
32. Parikshak, N. N. et al. Genome-wide changes in lncRNA, splicing, and regional gene expression patterns in autism. *Nature* **540**, 423–427 (2016).
33. Gandal, M. J. et al. Shared molecular neuropathology across major psychiatric disorders parallels polygenic overlap. *Science* **359**, 693–697 (2018).
34. Xie, J. et al. Long-term, efficient inhibition of microRNA function in mice using rAAV vectors. *Nat. Methods* **9**, 403–409 (2012).
35. Menkes-Caspi, N. et al. Pathological tau disrupts ongoing network activity. *Neuron* **85**, 959–966 (2015).
36. Zhang, B. et al. Integrated systems approach identifies genetic nodes and networks in late-onset Alzheimer's disease. *Cell* **153**, 707–720 (2013).
37. Jones, L. et al. Convergent genetic and expression data implicate immunity in Alzheimer's disease. *Alzheimers Dement.* **11**, 658–671 (2015).
38. Narayanan, M. et al. Common dysregulation network in the human prefrontal cortex underlies two neurodegenerative diseases. *Mol. Syst. Biol.* **10**, 743 (2014).
39. Dolmetsch, R. & Geschwind, D. H. The human brain in a dish: the promise of iPSC-derived neurons. *Cell* **145**, 831–834 (2011).
40. Hardy, J. Catastrophic cliffs: a partial suggestion for selective vulnerability in neurodegenerative diseases. *Biochem. Soc. Trans.* **44**, 659–661 (2016).
41. Gupta, S., Verma, S., Mantri, S., Berman, N. E. & Sandhir, R. Targeting microRNAs in prevention and treatment of neurodegenerative disorders. *Drug Dev. Res.* **76**, 397–418 (2015).
42. Janssen, H. L. A. et al. Treatment of HCV infection by targeting microRNA. *N. Engl. J. Med.* **368**, 1685–1694 (2013).
43. Young, D. D., Connelly, C. M., Grohmann, C. & Deiters, A. Small molecule modifiers of microRNA miR-122 function for the treatment of hepatitis C virus infection and hepatocellular carcinoma. *J. Am. Chem. Soc.* **132**, 7976–7981 (2010).
44. Allen, M. et al. Human whole genome genotype and transcriptome data for Alzheimer's and other neurodegenerative diseases. *Sci. Data* **3**, 160089 (2016).
45. Seyfried, N. T. et al. A multi-network approach identifies protein-specific co-expression in asymptomatic and symptomatic Alzheimer's disease. *Cell Syst.* **4**, 60–72.e4 (2017).
46. Prudencio, M. et al. Distinct brain transcriptome profiles in C9orf72-associated and sporadic ALS. *Nat. Neurosci.* **18**, 1175–1182 (2015).
47. Chang, L.-C. et al. A conserved BDNF, glutamate- and GABA-enriched gene module related to human depression identified by coexpression meta-analysis and DNA variant genome-wide association studies. *PLoS ONE* **9**, e90980 (2014).
48. Fromer, M. et al. Gene expression elucidates functional impact of polygenic risk for schizophrenia. *Nat. Neurosci.* **19**, 1442–1453 (2016).
49. Ferrari, R. et al. Frontotemporal dementia and its subtypes: a genome-wide association study. *Lancet Neurol.* **13**, 686–699 (2014).
50. Höglinger, G. U. et al. Identification of common variants influencing risk of the tauopathy progressive supranuclear palsy. *Nat. Genet.* **43**, 699–705 (2011).
51. Lambert, J.-C. et al. Meta-analysis of 74,046 individuals identifies 11 new susceptibility loci for Alzheimer's disease. *Nat. Genet.* **45**, 1452–1458 (2013).

Acknowledgements

Funding for this work was provided by Takeda Pharmaceuticals (D.H.G.), Rainwater Charitable Foundation/Tau consortium (D.H.G., S.J.H.), NIH grants to D.H.G., S.J.H.,

A.L. (5U01AG046161) and J.R. (5R25 NS065723) and Larry L. Hillblom Foundation Postdoctoral Fellowship to V.S. K.N., H.T., A.O., K.H. and S.K. are employees of Takeda Pharmaceuticals. The authors thank M. Hattori, Y. Obayashi and K. Nakamura for their contribution to the TPR50 mouse sample preparation and analysis. The authors thank M. Gearing at the Emory Alzheimer's Disease Research Center brain bank for providing human FTD samples. The authors also thank N. Parikshak for help with network analysis and critical reading of the manuscript. We thank Eli Lilly and Company scientists for generating the Tg4510 microglia RNA-seq data and providing access to them. For the PSP and FTD temporal cortex RNA-seq dataset, study data were provided by the following sources: Mayo Clinic Alzheimer's Disease Genetic Studies, led by N. Taner and S. G. Younkin, Mayo Clinic Jacksonville, using samples from the Mayo Clinic Study of Aging, Mayo Clinic Alzheimer's Disease Research Center, and Mayo Clinic Brain Bank. Data collection was supported through funding by National Institute on Aging (NIA) grants P50 AG016574, R01 AG032990, U01 AG046139, R01 AG018023, U01 AG006576, U01 AG006786, R01 AG025711, R01 AG017216, R01 AG003949, National Institute of Neurological Disorders and Stroke (NINDS) grant R01 NS080820, the CurePSP Foundation, and support from the Mayo Foundation. Study data include samples collected through the Sun Health Research Institute Brain and Body Donation Program of Sun City, Arizona. The Brain and Body Donation Program is supported by the NINDS (U24 NS072026 National Brain and Tissue Resource for Parkinson's Disease and Related Disorders), the NIA (P30 AG19610 Arizona Alzheimer's Disease Core Center), the Arizona Department of Health Services (contract 211002, Arizona Alzheimer's Research Center), the Arizona Biomedical Research Commission (contracts 4001, 0011, 05-901 and 1001 to the Arizona Parkinson's Disease Consortium) and the Michael J. Fox Foundation for Parkinson's Research. Tg4510 replication and CRND8 RNA-seq data were provided by the NIH U01 AG046139. We thank J. Lewis, K. Duff, D. Westaway and D. Borchelt for generating these lines of transgenic mice and providing access to them.

Author contributions

V.S. and D.H.G. planned and directed the experiments, guided the analysis and wrote the manuscript in conjunction with F.I.H. and J.E.R. All authors revised and edited the final version of the manuscript. F.I.H. performed all the experiments in mouse cortical cultures. V.S. performed all the bioinformatic analyses and performed dissections on human postmortem samples and isolated RNA. K.N., H.T., A.O., K.H. and S.K. bred the TPR50 mouse, characterized the F1 hybrids and collected the tissue samples. J.E.R. performed bioinformatic analysis using purified glial cells. J.E.R. and A.S. stained for and quantified inflammation in mouse brain samples. IFGC consortia members collected and analyzed FTD GWAS data. N.T.S., J.J.L. and A.I.L. performed mass spectrometry–based quantitative proteomics on human FTD samples obtained from M.G., V.M.V.D. and J.Q.T. The SAHA experiments were performed by C.C. and S.J.H. on human iPSC-derived neurons from tau and control patients.

Competing interests

D.H.G. has received research funding from Takeda Pharmaceutical Company Limited. K.N., H.T., A.O., K.H. and S.K. are employees of Takeda Pharmaceutical Company Limited.

Additional information

Supplementary information is available for this paper at https://doi.org/10.1038/s41591-018-0223-3.

Reprints and permissions information is available at www.nature.com/reprints.

Correspondence and requests for materials should be addressed to D.H.G.

Publisher's note: Springer Nature remains neutral with regard to jurisdictional claims in published maps and institutional affiliations.

International Frontotemporal Dementia Genomics Consortium

Raffaele Ferrari[12], Jonathan D. Rohrer[12], Adaikalavan Ramasamy[12], John Hardy[12], Dena G. Hernandez[13], Michael A. Nalls[13], Andrew B. Singleton[13], John B. J. Kwok[14], Carol Dobson-Stone[14], William S. Brooks[14], Peter R. Schofield[14], Glenda M. Halliday[14], John R. Hodges[14], Olivier Piguet[14], Lauren Bartley[14], Elizabeth Thompson[15], Eric Haan[15], Isabel Hernández[16], Agustín Ruiz[16], Mercè Boada[16], Barbara Borroni[17], Alessandro Padovani[17], Nigel J. Cairns[18], Carlos Cruchaga[18], Giuliano Binetti[19], Roberta Ghidoni[19], Luisa Benussi[19], Gianluigi Forloni[20], Diego Albani[20], Daniela Galimberti[21,22], Chiara Fenoglio[21,22], Maria Serpente[21,22], Elio Scarpini[21,22], Jordi Clarimón[23], Alberto Lleó[23], Rafael Blesa[23], Maria Landqvist Waldö[24], Karin Nilsson[24], Christer Nilsson[24], Ian R. A. Mackenzie[25], Ging-Yuek R. Hsiung[25], David M. A. Mann[26], Jordan Grafman[27], Christopher M. Morris[28], Johannes Attems[28], Timothy D. Griffiths[28], Ian G. McKeith[28], Alan J. Thomas[28], Evelyn Jaros[28], Pietro Pietrini[29], Edward D. Huey[30], Eric M. Wassermann[31], Michael C. Tierney[31], Atik Baborie[32], Pau Pastor[33], Sara Ortega-Cubero[33], Cristina Razquin[34], Elena Alonso[34], Robert Perneczky[35], Janine Diehl-Schmid[36], Panagiotis Alexopoulos[36], Alexander Kurz[36], Innocenzo Rainero[37], Elisa Rubino[37], Lorenzo Pinessi[37], Ekaterina Rogaeva[38], Peter St. George-Hyslop[38], Giacomina Rossi[39], Fabrizio Tagliavini[39], Giorgio Giaccone[39], James B. Rowe[40], Johannes C. M. Schlachetzki[41], James Uphill[42], John Collinge[42], Simon Mead[42], Adrian Danek[43], Vivianna M. Van Deerlin[8], Murray Grossman[7], John Q. Trojanowski[8], Stuart Pickering-Brown[44], Parastoo Momeni[45], Julie van der Zee[46], Marc Cruts[46], Christine Van Broeckhoven[46], Stefano F. Cappa[47], Isabelle Leber[48], Alexis Brice[48], Didier Hannequin[49], Véronique Golfier[50], Martine Vercelletto[51], Benedetta Nacmias[52], Sandro Sorbi[52], Silvia Bagnoli[52], Irene Piaceri[52], Jørgen E. Nielsen[53], Lena E. Hjermind[53], Matthias Riemenschneider[54], Manuel Mayhaus[54], Gilles Gasparoni[54], Sabrina Pichler[54], Bernd Ibach[55], Martin N. Rossor[56], Nick C. Fox[56], Jason D. Warren[56], Maria Grazia Spillantini[57], Huw R. Morris[58], Patrizia Rizzu[59], Peter Heutink[59], Julie S. Snowden[60], Sara Rollinson[60], Alexander Gerhard[60], Anna Richardson[61], Amalia C. Bruni[61], Raffaele Maletta[61], Francesca Frangipane[61], Chiara Cupidi[61], Livia Bernardi[61],

Maria Anfossi[61], Maura Gallo[62], Maria Elena Conidi[62], Nicoletta Smirne[62], Rosa Rademakers[63], Matt Baker[63], Dennis W. Dickson[63], Neill R. Graff-Radford[63], Ronald C. Petersen[64], David Knopman[64], Keith A. Josephs[64], Bradley F. Boeve[64], Joseph E. Parisi[65], Bruce L. Miller[66], Anna M. Karydas[66], Howard Rosen[66], William W. Seeley[67], John C. van Swieten[68], Elise G. P. Dopper[68], Harro Seelaar[68], Yolande A. L. Pijnenburg[69], Philip Scheltens[69], Giancarlo Logroscino[70], Rosa Capozzo[70], Valeria Novelli[71], Annibale A. Puca[72,73], Massimo Franceschi[74], Alfredo Postiglione[75], Graziella Milan[76], Paolo Sorrentino[76], Mark Kristiansen[77], Huei-Hsin Chiang[78], Caroline Graff[78], Florence Pasquier[79], Adeline Rollin[79], Vincent Deramecourt[79], Thibaud Lebouvier[79], Luigi Ferrucci[80] and Dimitrios Kapogiannis[81]

[12]Department of Molecular Neuroscience, University College London (UCL), London, UK. [13]Laboratory of Neurogenetics, National Institute on Aging, National Institutes of Health, Bethesda, MD, USA. [14]Neuroscience Research Australia, Sydney, New South Wales, Australia. [15]South Australian Clinical Genetics Service, Women's and Children's Hospital, Adelaide, South Australia, Australia. [16]Research Center and Memory Clinic of Fundació ACE, Institut Català de Neurociències Aplicades, Barcelona, Spain. [17]Neurology Clinic, University of Brescia, Brescia, Italy. [18]Hope Center, Washington University School of Medicine, St. Louis, MO, USA. [19]IRCCS Istituto Centro San Giovanni di Dio – Fatebenefratelli, Brescia, Italy. [20]Biology of Neurodegenerative Disorders, IRCCS Istituto di Ricerche Farmacologiche, Milan, Italy. [21]University of Milan, Milan, Italy. [22]Fondazione IRCCS Cà Granda, Ospedale Maggiore Policlinico, Milan, Italy. [23]Memory Unit, Neurology Department and Sant Pau Biomedical Research Institute, Hospital de la Santa Creu i Sant Pau, Universitat Autònoma de Barcelona, Barcelona, Spain. [24]Unit of Geriatric Psychiatry, Department of Clinical Sciences, Lund University, Lund, Sweden. [25]Department of Pathology and Laboratory Medicine, University of British Columbia, Vancouver, Canada. [26]Institute of Brain, Behaviour and Mental Health, University of Manchester, Salford Royal Hospital, Salford, UK. [27]Departments of Physical Medicine and Rehabilitation, Psychiatry, and Cognitive Neurology and the Alzheimer's Disease Center, Feinberg School of Medicine, Northwestern University, Chicago, IL, USA. [28]Institute for Ageing, Newcastle University, Newcastle-upon-Tyne, UK. [29]IMT School for Advanced Studies, Lucca, Lucca, Italy. [30]Taub Institute, Departments of Psychiatry and Neurology, Columbia University, New York, NY, USA. [31]Behavioral Neurology Unit, National Insititute of Neurological Disorders and Stroke, Bethesda, MD, USA. [32]Department of Laboratory Medicine & Pathology, University of Alberta, Edmonton, Alberta, Canada. [33]Center for Networker Biomedical Research in Neurodegenerative Diseases (CIBERNED), Madrid, Spain. [34]Neurogenetics Laboratory, Division of Neurosciences, Center for Applied Medical Research, Universidad de Navarra, Pamplona, Spain. [35]Neuroepidemiology and Ageing Research Unit, School of Public Health, Imperial College of Science, Technology and Medicine, London, UK. [36]Department of Psychiatry and Psychotherapy, Technische Universität München, Munich, Germany. [37]Department of Neuroscience, University of Torino, Turin, Italy. [38]Tanz Centre for Research in Neurodegenerative Diseases, University of Toronto, Toronto, Ontario, Canada. [39]Division of Neurology V and Neuropathology, Fondazione IRCCS Istituto Neurologico Carlo Besta, Milan, Italy. [40]Cambridge University Department of Clinical Neurosciences, Cambridge, UK. [41]Department of Cellular & Molecular Medicine, University of California San Diego, La Jolla, CA, USA. [42]MRC Prion Unit, Department of Neurodegenerative Disease, UCL Institute of Neurology, London, UK. [43]Neurologische Klinik und Poliklinik, Ludwig-Maximilians-Universität, Munich, Germany. [44]Institute of Brain, Behaviour and Mental Health, Faculty of Medical and Human Sciences, University of Manchester, Manchester, UK. [45]Laboratory of Neurogenetics, Department of Internal Medicine, Texas Tech University Health Science Center, Lubbock, TX, USA. [46]Neurodegenerative Brain Diseases group, Department of Molecular Genetics, VIB, Antwerp, Belgium. [47]Neurorehabilitation Unit, Department of Clinical Neuroscience, Vita-Salute University and San Raffaele Scientific Institute, Milan, Italy. [48]Inserm, CRICM, Paris, France. [49]Service de Neurologie, Rouen University Hospital, Rouen, France. [50]Service de Neurologie, CH, Saint-Brieuc, France. [51]Service de Neurologie, CHU, Nantes, France. [52]Department of Neurosciences, Psychology, Drug Research and Child Health (NEUROFARBA), University of Florence, Florence, Italy. [53]Danish Dementia Research Centre, Neurogenetics Clinic, Department of Neurology, Rigshospitalet, Copenhagen University Hospital, Copenhagen, Denmark. [54]Saarland University Hospital, Laboratory for Neurogenetics, Homburg (Saar), Germany. [55]Department of Psychiatry, Psychotherapy and Psychosomatics, University Regensburg, Regensburg, Germany. [56]Dementia Research Centre, Department of Neurodegenerative Disease, UCL Institute of Neurology, London, UK. [57]Department of Clinical Neurosciences, John Van Geest Brain Repair Centre, University of Cambridge, Cambridge, UK. [58]Department of Molecular Neuroscience, UCL, London, UK. [59]German Center for Neurodegenerative Diseases-Tübingen, Tübingen, Germany. [60]Institute of Brain, Behaviour and Mental Health, Faculty of Medical and Human Sciences, University of Manchester, Manchester, UK. [61]Salford Royal Foundation Trust, Faculty of Medical and Human Sciences, University of Manchester, Manchester, UK. [62]Regional Neurogenetic Centre, ASPCZ, Lamezia Terme, Italy. [63]Department of Neuroscience, Mayo Clinic Jacksonville, Jacksonville, FL, USA. [64]Department of Neurology, Mayo Clinic Rochester, Rochester, MN, USA. [65]Department of Pathology, Mayo Clinic Rochester, Rochester, MN, USA. [66]Memory and Aging Center, Department of Neurology, University of California, San Francisco, CA, USA. [67]Department of Neurology, University of California, San Francisco, CA, USA. [68]Department of Neurology, Erasmus Medical Centre, Rotterdam, The Netherlands. [69]Alzheimer Centre and Department of Neurology, VU University Medical Centre, Amsterdam, The Netherlands. [70]Department of Basic Medical Sciences, Neurosciences and Sense Organs, University of Bari Aldo Moro, Bari, Italy. [71]Medical Genetics Unit, Fondazione Policlinico Universitario Agostino Gemelli, Rome, Italy. [72]Cardiovascular Research Unit, IRCCS Multimedica, Milan, Italy. [73]Department of Medicine and Surgery, University of Salerno, Baronissi, Italy. [74]Neurology Department, IRCCS Multimedica, Milan, Italy. [75]Department of Clinical Medicine and Surgery, University of Naples Federico II, Naples, Italy. [76]Geriatric Center Frullone-ASL Napoli 1 Centro, Naples, Italy. [77]UCL Genomics, Institute of Child Health (ICH), UCL, London, UK. [78]Department NVS, Alzheimer Research Center, Karolinska Institutet, Novum, Stockholm, Sweden. [79]University of Lille, Lille, France. [80]Clinical Research Branch, National Institute on Aging, Baltimore, MD, USA. [81]Cellular and Molecular Neuroscience Section, National Institute on Aging, Baltimore, MD, USA.

Methods

Animals. TPR50 mice were generated in the C57BL/6J background and maintained at the Shonan Research Center, Fujisawa City, Japan as described previously[13]. TPR50 mice overexpress the tau^{P301S} (4R2N isoform) under the control of a mouse prion promoter. Mice were outbred to DBA/2J and FVB/NJ strains. Heterozygous F1 male mice (at 3 and 6 months of age) were used to collect brain tissues (cortex, hippocampus, brain stem and cerebellum) for immunohistochemical staining and RNA isolation. WT littermates of the same genetic background and age were used as controls. All procedures involving animals were performed in accordance with the University of California, Los Angeles animal research committee, the National Institutes of Health (NIH) *Guide for the Care and Use of Laboratory Animals* and by the Experimental Animal Care and Use Committee of Takeda Pharmaceutical Company Limited, Japan. WT C57BL/6J mice were directly purchased from Jackson Laboratories.

Human postmortem brain samples. Postmortem brain tissue from human FTD and control individuals used for mRNA (mRNA-seq) and miRNA sequencing (miRNA-seq) were acquired from the Emory Alzheimer's Disease Research Center brain bank at Emory University School of Medicine. Human postmortem tissues were acquired under Emory University Institutional Review Board with consent from family members. Sample acquisition protocols approved by the University of California, Los Angeles Institutional Review Board were followed, and samples were deidentified before acquisition. Brain sample information and individual-level metadata are available in Supplementary Table 2b. Proteomics samples were obtained from Penn Alzheimer's Disease Research Center as part of the Accelerating Medicine Partnership for Alzheimer's Disease; sample-level metadata are available in Supplementary Table 2c.

Immunohistochemistry/immunofluorescence. Paraffin-embedded mouse brain samples were briefly deparaffinized and blocked in 5% serum. Sections were stained overnight with phospho-tau (Ser202, Thr205) AT8 clone (Thermo Fisher Scientific) at 1:250 dilution followed by incubation in biotinylated secondary antibody and imaged under microscope. For immunofluorescence, sections were stained with an antibody raised against GFAP (Dako; 1:500) or Iba-1 (Wako; 1:500) followed by incubation in Alexa Fluor 488 or 594 secondary antibody (Invitrogen; 1:500) for 1 h at room temperature and counterstained with DAPI. Images were obtained either with a ZEISS Axio Imager or on a digital slide scanner NanoZoomer 2.0-HT (Hamamatsu Photonics K.K.).

mRNA-seq and miRNA-seq. A quantity of 1 µg total RNA was used for mRNA-seq and miRNA-seq. For mRNA-seq, polyA-selected mRNAs were processed for unstranded libraries using the TruSeq V2 kit (Illumina) that underwent 50-bp paired-end sequencing on an Illumina HiSeq 2500 system. Paired-end reads were mapped to the reference mouse NCBIM37 genome using TopHat2 and Ensembl release 67 annotations (May 2012 data freeze). Count-level data were quantified using union gene models with HTSeq-counts. For miRNA-seq, a second sample from the same total RNA fraction was used, and libraries were prepared using the TruSeq Small RNA Library Prep Kit (Illumina). The 50-bp single-end reads were processed for miRNA expression using the miRDeep2 analysis pipeline.

Coexpression network analysis. Coexpression network analysis was performed in R using the WGCNA package[16]. To identify mRNA modules that are conserved across various Tg mouse strains, we used a consensus network analysis (WGCNA) approach. To identify common expression patterns across genetic backgrounds, we created a signed consensus network for each brain region individually by calculating component-wise minimum values for topological overlap across different mouse strains. For miRNA data, we performed WGCNA analysis using signed networks.

Mouse embryonic cortical cell culture. Cortical tissue from day 15 (E15) C57BL/6J embryos was collected, dissected and washed in ice-cold Hank's balanced salt solution (HBSS; Invitrogen). Tissue was incubated in 0.25% trypsin (Invitrogen) in the presence of DNase I (Roche) at 37 °C for 10 min. Tissue was washed with cold HBSS and triturated in plating media (Gibco Neurobasal Medium; Thermo Fisher Scientific), 20% heat-inactivated horse serum (Thermo Fisher Scientific), 25 mM sucrose and 0.25% Gibco GlutaMAX (Thermo Fisher Scientific) in the presence of DNase I. Dissociated cells were centrifuged at 125*g* for 5 min at 4 °C, resuspended in plating medium, counted and plated in poly-L-lysine-coated (Sigma-Aldrich) plates at a density of 300,000 cells ml^{-1}. If cells were infected with miRNA-203 or scrambled control lentiviral constructs (Systems Biosciences; MMIR203-PA-1), 10 IFU per cell was added to the suspended cells before plating. Plating medium was replaced 24 h after plating with Neurobasal Medium supplemented with 1% B-27 supplement (Thermo Fisher Scientific) and 0.25% Gibco GlutaMAX.

Stereotactic injection of AAV2/9 into mouse brain. Mice were anesthetized with isoflurane and head-fixed over a heating pad set to 37 °C. Craniotomy was performed according to approved procedures (animal protocol number 2000-159). The eyes were covered with artificial teardrops, the scalp was bisected and the exposed area was sterilized on a stereotactic frame (Model 900 Small Animal Stereotaxic Instrument; David Kopf Instruments). The skull was thinned using a Dremel drill, and 1 µl of AAV 2/9 (1×10^{13} vector genomes ml^{-1} of hSyn-miR203-hSyn-enhanced green fluorescent protein (eGFP); 1×10^{13} vector genomes ml^{-1} of hSyn-scrambled:miRNA-hSyn-eGFP (SignaGen Laboratories)) was injected bilaterally into the frontal cortex (anterior/posterior: +2.1 mm; mediolateral: ± 1.5 mm; dorsal/ventral: −2.5 mm) at a rate of 100 nl min^{-1} using a Hamilton 5-µl syringe (Hamilton Company). Before each injection, the pipette was lowered 0.1 mm beyond the intended target depth and held in place for 3 min to create space for the injected solution; after each injection, the pipette was held in place for 7 min before retraction to prevent leakage. The incision was sterilized and glued, and postoperative antibiotics (amoxicillin, 50 mg ml^{-1}) were administered for 7 d following surgery.

Sample collection and RNA isolation. TPR50 mice at 3 and 6 months of age were killed using cervical dislocation. The cortex, hippocampus, brain stem and cerebellum were dissected on ice-cold PBS buffer solution and flash-frozen to minimize RNA degradation. RNA was isolated from different brain regions of interest from each sample using the miRNeasy kit with on column DNase digestion (QIAGEN) using a QIAcube automated system. For each RNA sample, the RNA concentration was determined using a Quant-iT RiboGreen RNA Assay Kit (Invitrogen), and RNA integrity was quantified using the RNA integrity number (RIN)[52] on an Agilent 2200 TapeStation.

Frozen human brain samples obtained from Emory brain bank were dissected on dry ice in a dehydrated dissection chamber to reduce degradation effects from sample thawing or humidity; 50–100 mg tissue samples were used to isolate RNA using the miRNeasy kit with on column DNase digestion; samples with RIN > 2 were used further.

Mouse primary cortical neurons were washed with ice-cold RNase-free PBS; QIAzol lysis reagent (QIAGEN) was immediately added to the 6-well plates. RNA was isolated using the miRNeasy kit according to the manufacture's protocol.

Several datasets have been used throughout the study, details of which can be found in Supplemental Table 2a. Mouse datasets consist of: Tg4510 (ref. [53]); PS2APP[54]; CRND8 (ref. [55]); APP/PS1 (ref. [56]); GRN[57]. Human postmortem data consist of: AD temporal cortex[44]; AD frontal cortex[46]; AD proteomics[45]; pathological aging without dementia[44]; ALS[46]; PSP[44]; major depression[47]; schizophrenia and bipolar disorder[48].

Enzyme-linked immunosorbent assay. Total tau and pT231 tau content were measured by commercial tau ELISA kits according to the manufacturer's instructions (total tau, KHB0041; pT231 tau, KHB8051; Invitrogen). Briefly, standards, radioimmunoprecipitation assay-soluble or sarkosyl-insoluble samples were applied to the ELISA plate. After washing, a biotin-conjugated detection antibody was applied. The positive reaction was enhanced with streptavidin–horseradish peroxidase and colored by 3,3′,5,5′-tetramethylbenzidine. The absorbance at 450 nm was then measured, and the concentration of tau protein was calculated from the standard curve.

RNA-seq library preparation. For the TPR50 mouse data, 1 µg of total RNA was used to obtain poly(A)-selected mRNAs, which were processed for unstranded libraries using the TruSeq RNA Sample Prep v2 kit (Illumina). Briefly, the poly(A) tail–containing mRNA was isolated using oligo-dT-attached magnetic beads; mRNA was fragmented and first-strand complementary DNA (cDNA) was generated using SuperScript II Reverse Transcriptase (Invitrogen) followed by second-strand cDNA generation. Barcodes and adapters were added and subsequent steps followed the TruSeq protocol to generate fragment sizes (150–500 bp; mean, 250 bp). The libraries were quantified with the Quant-iT PicoGreen assay (Thermo Fisher Scientific) and validated on an Agilent 2200 TapeStation system. Libraries were multiplexed with 24 samples per lane, and each lane was sequenced several times to get an average read depth of 40–50 million reads per sample on an Illumina HiSeq 2500 instrument using a high-output mode with standard chemistry and protocols for 50-bp paired-end reads.

For postmortem human data, 1 µg of total RNA was used for ribosomal RNA (rRNA) depletion with the Ribo-Zero Gold Kit (Illumina). Remaining RNA was size-selected using AMPure XP beads (Beckman Coulter), and standard libraries were prepared following Illumina's TruSeq protocols for 50-bp paired-end reads. Libraries were sequenced at an average read depth of 60–70 million reads per sample on a HiSeq 2500 instrument using rapid mode.

We used a SMART-Seq v4 Ultra Low Input RNA Kit (Clontech) for the library preparation of fluorescence-activated cell sorting (FACS)-sorted adult mouse neurons. RNA from FACS-sorted cells (~1,000 cells) were isolated with the NucleoSpin RNA XS kit (Clontech) with on column DNase digestion according to the manufacturer's protocol; the RNA was eluted in 10 µl of RNase-free water. rRNA was depleted from the eluted total RNA, and cDNA was synthesized using PrimeScript Reverse transcriptase (Clontech). Sequencing adapters were added, and the library was amplified using SeqAmp DNA Polymerase (Clontech). Strand-specific library was size-selected using AMPure XP beads and validated for fragment sizes (200–1000 bp, peaking at 300 bp). Libraries were multiplexed with 12 samples per lane, and each library was sequenced several times to get an average

read depth of 30–40 million reads per sample on a HiSeq 2500 instrument using rapid mode.

We used TruSeq Stranded RNA-seq (Illumina) for the library preparation of vorinostat-treated neurons. Briefly, cell pellet was collected from 6-well plates, and RNA was isolated using miRNeasy kit with on column DNase digestion; 100 ng of total RNA was used for downstream library preparation according to the manufacturer's recommended protocol. Libraries were multiplexed with 24 samples per lane, and each library was sequenced several times to get an average read depth of 30–40 million reads per sample on a HiSeq 4000 system.

mRNA-seq read alignment and processing. To analyze the TPR50 mouse mRNA-seq data, the paired-end raw reads were mapped to the reference mouse NCBIM37 genome using Ensembl release 67 (May 2012 data freeze) annotations with TopHat2 (version 2.0.5)[58] with the novel junction option turned off. Aligned reads were sorted, and alignments mapped to different chromosomes were removed from the BAM file using SAMtools[59]. Gene expression levels were quantified for all the samples using union gene models with HTSeq-counts (version 0.5.4)[60], which uses uniquely aligned reads. Genes were included in the analysis if they were expressed in 80% of the samples with >10 reads. It is common practice in RNA-seq experiments to filter low-expressed genes[32,61]. There are a few reasons for this: (i) low-expressed genes are not reliably quantified and thus vary significantly between biological replicates; (ii) none of the models such as the negative binomial distribution from DESeq2 (or edgeR), or $\log_2$ transformation followed by linear regression (which we used), can effectively model such highly variable genes. Because of these reasons, we removed these genes, mainly to reduce noise in gene expression, from the RNA-seq experiments.

The resulting read counts were normalized for library size using the 'cpm' function of the egdeR package in R[62] to get fragments per kilobase million mapped reads (FPKM) values. $\log_2$-transformed FPKM values were quantile-normalized using the 'betweenLaneNormalization' function of the EDAseq package in R[63].

For postmortem human data, the paired-end strand-specific reads were mapped to the reference human GRCh37.73 (Gencode 19) genome using the RNA-STAR aligner (version 2.4.2a)[64]. Count-level data were quantified using union gene and union exon models with HTSeq-counts (version 0.6.1); genes were kept if they were expressed in 80% of the samples with >10 reads with HTSeq quantifications. Read counts were $\log_2$-transformed; guanine-cytosine content, gene-length and library-size-normalized FPKM values were obtained using the cqn package in R[65].

FACS-sorted neuronal RNA-seq data were processed similarly to the human RNA-seq data except that the paired-end reads were mapped to the reference mouse NCBIM37 genome with Ensembl release 67 annotations using the RNA-STAR aligner (version 2.4.2a).

miRNA-seq read alignment and processing. Mouse and human miRNA-seq read alignments and quantifications were performed using the miRDeep2 package[66]. We used the mapper.pl script to map the 50-bp single-end reads to the reference genome, NCBIM37 for mouse and GRCh37 for human. We then used the quantifier.pl script of the package to map the reads to annotated miRNAs, which were downloaded from the miRBase (version 20 for mouse data and miRbase version 21 for human data) website (see URLs). The script gives a count-level quantification of each known miRNA; we used the quantile-normalized values as provided by the script for downstream analyses.

Microarray: mouse embryonic cortical cells. Total RNA isolated from E15 cortical cultures using the miRNeasy Mini Kit (QIAGEN) were processed on a mouse Ref8 v2 BeadChip microarray (Illumina) according to the manufacturer's protocol. Microarray data analysis was performed with the R and Bioconductor packages. Raw expression data were $\log_2$-transformed and normalized by quantile normalization. Probes were considered robustly expressed if the detection P value was 0.05 for at least half of the samples in the dataset. Probes were remapped to mouse Ensembl gene IDs (version 67; May 2012 data freeze) for comparison with RNA-seq data.

Differential gene expression. We used principal component analysis (PCA) of the normalized gene expression data to understand the biological and technical covariates effecting the data. For the TPR50 dataset, we found that none of the first five gene expression PCAs correlated significantly with the batch or sequencing PCAs. Thus, we only performed differential expression within a brain region and separately for each age group using the normalized FPKM values in the linear regression model in R as follows:

$$\text{lm}(\text{expression} \sim \text{Transgenic}.\text{Condition} + \text{MouseStrain} + \text{Sequencing}.\text{Lane}.\text{Batch} + \text{RIN})$$

For all other mouse datasets, RIN, the first two sequencing PCAs, batch and experimental batch were used as the covariates in the linear regression model. For the human data, additional traits like age, sex and postmortem interval (PMI) were also used for the analysis. We also performed differential gene expression for the TPR50 dataset using the DESeq2 R package[67] using raw counts data from HTSeq-counts following the default parameters and taking transgenic condition, mouse strain, sequencing lane batch and RIN as covariates for the DESeq2 regression.

mRNA-weighted coexpression network analysis. Coexpression network analysis was performed using a user-friendly R WGCNA library[16]. We wanted to investigate mouse brain coexpression networks that are disease-specific but are independent of genetic backgrounds (C57BL6/J, DBA and FVB). Thus, we used a consensus network analysis approach, which provided us with groups of coexpressed genes (or modules) that are not affected by mouse genetic background. TPR50 mice were generated using a bacterial artificial chromosome clone as the transgene, which overexpressed P301S mutation in the human *MAPT* gene (4R2N isoform). However, the bacterial artificial chromosome clone had three additional confounding genes, *Prnd*, *Erv3* and *Rassf2* in the construct, which were also overexpressed. To remove the effect of the confounding genes, we took the first principal component of the expression of the confounding genes and removed the genes, which are significantly correlated at a false discovery rate (FDR) of $P<0.05$. This resulted in the removal of about 1,000 genes, which are highly correlated with the confounding genes. We only used the 6-month time point to construct the initial network. The resulting expression data for each brain region, except for the cerebellum, at the 6-month time point was used to create the consensus network separately; the 'matchLabels' function of the WGCNA package was used to have consistent network labeling between brain regions.

In short, biweighted midcorrelations were calculated for all pairs of genes, and then a signed similarity matrix was created. In the signed network, the similarity between genes reflects the sign of the correlation of their expression profiles. The signed similarity matrix was then raised to the power β to emphasize strong correlations and reduce the emphasis of weak correlations on an exponential scale. The resulting adjacency matrix was then transformed into a topological overlap matrix as described here[68].

Since we are primarily interested in finding coexpression patterns conserved across different mouse genetic backgrounds, we created a consensus network to identify common coexpression patterns across strains, following published methods[69]. After scaling for each individual network (consensus scaling quantile = 0.2), a threshold power of 12 was chosen (because it was the smallest threshold that resulted in a scale-free R^2 fit of 0.8) and the consensus network was created by calculating the component-wise minimum values for topological overlap. Using 1 − TO (dissTOM) as the distance measure, genes were hierarchically clustered. Initial module assignments were determined using a dynamic tree-cutting algorithm (cutreeHybrid, using the default parameters except deepSplit = 4, cutHeight = 0.999, minModuleSize = 100, dthresh = 0.1 and pamStage = FALSE).

The resulting modules or groups of coexpressed genes were used to calculate the MEs or the first principal component of the module. Modules were annotated with the GO-Elite package[70]. We performed module preservation analysis using mRNA module definitions. MEs were correlated with different biological and technical traits like transgenic condition, strain and RIN to find disease-specific modules. Module hubs were defined by calculating module membership (kME) values, which are the Pearson correlations between each gene and each ME. Genes with a kME < 0.7 were removed from the module. Network visualization was done with the igraph package in R[71]. Module definitions from the network analysis were used to create synthetic eigengenes for the 3-month time point and were used to understand the trajectory of various modules across time points. For the cerebellum, a data synthetic ME was calculated using cortex coexpression definitions and plotted.

Cell-type-specific regression analysis. To ensure that the changes in module expression identified were not solely a product of neurodegeneration and gliosis, we employed a multivariate linear regression model to regress gene expression levels against transgenic condition and the first principal component (PC1) of the top 100 cell-type-specific marker genes[72] for five major cell types: neurons; astrocytes; oligodendrocytes; microglia; and endothelial cells. This method removes the confounding effect of changes in cell composition (for example, see refs [19,20]):

$$\text{lm}(\text{geneExpression} \sim \text{TransgenicCondition} + \text{PC1.Neurons} + \text{PC1.Astrocytes} + \text{PC1.Microglia} + \text{PC1.Oligodendrocytes} + \text{PC1.EndothelialCells})$$

Module preservation analysis. We used module preservation analysis to validate coexpression in independent mouse and human datasets. Module definitions from the TPR50 consensus network analysis were used as reference and the analysis was used to calculate the z-summary statistic for each module. This measure combines module density and intramodular connectivity metrics to give a composite statistic where $z>2$ suggests modest preservation and $z>10$ suggests high preservation[73].

Enrichment analyses for gene sets. Gene set enrichment analysis was performed using a two-tailed Fisher's exact test with 95% confidence intervals calculated

according to the R function fisher.test. We used *P* values from this two-tailed approach for the one-tailed test (which is equivalent to the hypergeometric *P* value) because we do not assume enrichment a priori[74]. To reduce false positives, we used FDR-adjusted *P* values[75] for multiple hypergeometric test comparisons. For cell-type enrichment analysis, we used an already published mouse brain dataset[22]. The background for overrepresentation analysis was chosen as brain region-expressed data from our RNA-seq data.

For miRNA binding site/target enrichment analysis, we downloaded predicted miRNA targets from the mouse TargetScan database (version 6.2; see URLs) using only conserved predicted targets[76]. For background we used all genes expressed in the mouse genome.

Genes in network modules were characterized using GO-Elite (version 1.2.5), using the brain-region-expressed genes as background[70]. GO-Elite uses a *z*-score approximation of the hypergeometric distribution to assess term enrichment and removes redundant gene ontology or Kyoto Encyclopedia of Genes and Genomes terms to give a concise output. We used 10,000 permutations and required at least 10 genes to be enriched in a given pathway at a *z*-score of at least 2. We report only the biological process and molecular function category output.

PPI analysis. We used two PPI resources, InWeb[77] and BioGRID[22]. Basic analysis was performed similarly to methods published elsewhere[23]. Using the union of the two resources, the subset of compiled PPIs between genes in a module was extracted and all edges were counted. The PPI dataset was matrix-multiplied with coexpression data from RNA-seq (as earlier); edges that were present both in PPI and coexpression datasets were eventually kept. This approach allowed us to infer tissue and species specificity in the PPI network. The PPI network was then visualized using the igraph package in R. We also assessed whether the modules were interconnected by PPIs above a chance level with DAPPLE[77], which uses a within-degree within-node permutation method that allows us to rank PPI hubs by *P* value.

miRNA-weighted coexpression network analysis. The miRNA coexpression networks for each brain region, except the cerebellum, at the 6-month time point were constructed separately using the R package WGCNA as described previously[78]. A threshold power of 12 was chosen (because it was the smallest threshold that resulted in a scale-free R^2 fit of 0.8). The network was created by calculating the component-wise minimum values for topological overlap and miRNAs were hierarchically clustered. Initial module assignments were determined by using a dynamic tree-cutting algorithm (cutreeHybrid function, using default parameters except deepSplit = 2, cutHeight = 0.999, minModuleSize = 40, dthresh = 0.1 and pamStage = FALSE). Other steps were similar to mRNA coexpression analysis described earlier. Module definitions from the network analysis were used to create synthetic eigengenes for the 3-month time point and were used to understand the trajectory of various modules across time points.

Label-free quantitative proteomics. Label-free quantitative proteomics were performed at the Emory Integrated Proteomics Core, Emory University, USA. Detailed methods are published elsewhere[58]. Briefly, postmortem frozen human brain samples were homogenized in urea lysis buffer (8 M urea, 100 mM $NaHPO_4$ buffer system, pH 8.5), including 5 µl (100× stock) Halt protease and phosphatase inhibitor cocktail (Thermo Fisher Scientific), and further diluted with 50 mM NH_4HCO_3 to a final concentration of less than 2 M urea and were then treated with 1 mM dithiothreitol at 25 °C for 30 min, followed by 5 mM iodoacetamide at 25 °C for 30 min in the dark. Protein was digested with 1:100 (wt/wt) lysyl endopeptidase (Wako) at 25 °C for 2 h and further digested overnight with 1:50 (wt/wt) trypsin (Promega Corporation) at 25 °C. The resulting peptides were desalted with a Sep-Pak C18 column (Waters) and dried under vacuum.

Brain-derived tryptic peptides (2 mg) were resuspended in peptide loading buffer (0.1% formic acid, 0.03% trifluoroacetic acid, 1% acetonitrile) containing 0.2 pmol of isotopically labeled peptide calibrants (Thermo Fisher Scientific). Peptide mixtures were separated on a self-packed C18 (1.9 µm; Dr. Maisch GmbH) fused-silica column (25 cm × 75 mM internal diameter; New Objective) by a nanoAcquity ultra-high performance liquid chromatography (Waters) and monitored on a Q Exactive Plus mass spectrometer (Thermo Fisher Scientific). Elution was performed over a 120-min gradient at a rate of 400 nl min^{-1} with buffer B ranging from 3 to 80% (buffer A: 0.1% formic acid and 5% dimethylsulfoxide (DMSO) in water; buffer B: 0.1% formic acid and 5% DMSO in acetonitrile). The mass spectrometer cycle was programmed to collect one full mass spectrometry (MS) scan followed by 10 data-dependent tandem MS (MS/MS) scans. The MS scans (300–1800 m/z range, 1,000,000 automatic gain control, 150 ms maximum ion time) were collected at a resolution of 70,000 at 200 m/z in profile mode and the MS/MS spectra (2 m/z isolation width, 25% collision energy, 100,000 automatic gain control target, 50 ms maximum ion time) were acquired at a resolution of 17,500 at 200 m/z. Dynamic exclusion was set to exclude previously sequenced precursor ions for 30 s within a 10 ppm window. Precursor ions with +1 and +6 or higher charge states were excluded from sequencing. The label-free quantitation algorithm in MaxQuant[79] was used for protein quantitation. The quantitation method only considered razor and unique peptides for protein-level quantitation. The label-free quantitation intensities were log_2-transformed for downstream analyses.

Lentivirus production. 10-cm dishes were coated in poly-L-ornithine (Sigma-Aldrich) diluted in PBS buffer solution and incubated at 37 °C for 1 h overnight. Plates were washed twice with PBS buffer solution. HEK 293T cells were seeded in DMEM supplemented with 10% fetal bovine serum (FBS; Invitrogen); 24 h after plating, medium was replaced with prewarmed DMEM, and HEK 293T cells were transfected with 9 µg purified lentiviral construct DNA, 9 µg purified PAX2 DNA and 0.9 ug purified VSVG DNA diluted in 1 ml Opti-MEM reduced serum medium (Invitrogen) and 60 µl lipofectamine 2000 transfection reagent (Invitrogen) diluted in 1 ml Opti-MEM. Four to six hours post-transfection, medium was removed and replaced with 10 ml prewarmed DMEM + 30% FBS; 16 h after medium exchange, medium was replaced with prewarmed DMEM + 10% FBS; 48 h following second medium exchange, medium was collected, centrifuged for 3 min at 3,000*g* at room temperature and filtered through a 0.45-µm filter. Virus was concentrated with the Lenti-X concentrator (Clontech) and resuspended in Gibco Neurobasal-A Medium (Thermo Fisher Scientific) supplemented with 5 ug ml^{-1} polybrene. Virus was titered with the Lenti-X p24 Rapid Titer Kit (Clontech), aliquoted and stored at −80 °C until used.

miRNA expression. Expression levels of individual miRNAs of interest were quantified using the QIAGEN miScript kits. For low-input miRNA quantification, miRCURY LNA Universal RT microRNA PCR system (Exiqon) was used, using primers specifically designed for miR-203.

Terminal deoxynucleotidyl transferase dUTP nick-end labeling (TUNEL) staining: mouse embryonic cortical cells. Embryonic cortical cultures were fixed with 4% paraformaldehyde (Electron Microscopy Sciences), washed with PBS and permeabilized in 0.25% Triton X-100 in PBS for 20 min at room temperature. For TUNEL staining, coverslips were washed with deionized water; double-stranded DNA breaks were labeled using the Click-iT TUNEL Alexa Fluor 594 Imaging Assay (Invitrogen). Nuclei were labeled with the Hoechst 33342 solution provided in the Click-iT TUNEL kit. Coverslips were mounted in Fluoromount-G (SouthernBiotech) and imaged with a ZEISS Axio Imager. The percentage of $TUNEL^+$ cells in each condition was determined as the number of $TUNEL^+$ cells over the total nuclei detected.

Isolation of infected adult mouse neurons using flow cytometry. The frontal cortex of adult male mice was dissected in ice-cold Hibernate A without calcium (HA − Ca; BrainBits). Tissue was roughly chopped in HA − Ca, moved to a 15-ml Falcon tube and incubated in 5 ml of activated papain (Worthington; resuspended in HA − Ca) in the presence of DNase I for 30 min at 37 °C with continuous agitation. Papain-digested tissue was triturated and cell debris was removed using ovomucoid (Worthington; resuspended in resuspended in HA − Ca) discontinuous density gradient centrifugation. The cell pellet was resuspended in 1.8 ml Hibernate A low fluorescence (HA-LF; BrainBits) to create a mononuclear cell suspension. To further reduce the amount of debris, the Miltenyi myelin removal kit was used. Briefly, 200 µl myelin removal beads (Miltenyi) were added to the cell suspension and incubated at 4 °C for 15 min, then 2 ml of HA-LF was added and the cell suspension was centrifuged at 300*g* for 10 min at 4 °C. The supernatant was aspirated, and the pellet was resuspended in 1 ml of HA-LF and applied to prepared LS columns (Miltenyi). Flow-through, as well as two 1 ml washes with HA-LF, were collected, centrifuged at 600*g* for 5 min at 4 °C and resuspended in 750 µl HA-LF. Myelin-depleted samples were labeled with live cell marker DRAQ5 (1 µl per 1 ml of cell suspension; Thermo Fisher Scientific) and dead cell marker NucBlue (2 drops ml^{-1} of cell suspension; Invitrogen). The cells were FACS-sorted on a Becton Dickinson FACS Aria cell sorter gating for $DAPI^-/DRAQ5^+/GFP^+$ cells. For each sample, a maximum of 1,000 cells were isolated and directly collected in 100 µl of RA1 lysis buffer with 2 µl tris(2-carboxyethyl)phosphine hydrochloride (TCEP); low-mass RNA was isolated with on column DNase digestion using the NucleoSpin RNA XS kit (Clontech) according to the manufacturer's protocol.

Immunohistochemistry. Three or six weeks after AAV-mediated infection, mice were anesthetized with sodium pentobarbital, 40 mg kg^{-1} body weight, and perfused intracardially, first with PBS and then followed by 4% paraformaldehyde in PBS. The brains were removed, postfixed overnight and cryoprotected by immersion in 30% sucrose in PBS for 48 h. Brains were embedded in optimum cutting temperature compound, sectioned at a thickness of 20 µm on a cryostat, mounted and used for IHC using standard protocols. Incubation with primary antibodies was performed overnight at 4 °C and with secondary antibodies for 60 min at room temperature. For primary antibodies, we used rabbit anti-GFP (1:500; Invitrogen) and rabbit anti-caspase-8 (1:800; Cell Signaling). Images were acquired with a ZEISS LSM 780 laser scanning confocal microscope (fluorescence) or ZEISS Axio Imager.

Western blot. E15 cortical cultures were washed in PBS, dissociated in 0.25% prewarmed trypsin, washed in PBS and pelleted by centrifugation at 1,500*g* for 1 min at room temperature. Cell pellets were resuspended in 50–70 µl Tris-NaCl-

Tween buffer (150 mM NaCl, 1 mM EDTA, 50 mM Tris pH 7.4, 1% Triton X-100) supplemented with protease and phosphatase inhibitors (Roche). Lysates were incubated at 4 °C for 30 min with constant agitation and centrifuged at 13,000*g* for 5 min at 4 °C. Supernatant was transferred to a new tube; protein concentration was measured using Bradford reagent (BioRad), and equal volumes of Laemmli sample buffer (BioRad) supplemented with β-mercaptoethanol were added to the lysate. Lysates were briefly heated to 95 °C, loaded onto 4–15% mini-PROTEAN TGX Precast Gels (BioRad) and run at 100 V for approximately 1.5 h. Samples were transferred to polyvinylidene difluoride membranes (BioRad), blocked with 5% milk or 3% bovine serum albumin (BSA) in PBS with Tween 20 for 1 h at room temperature, probed with primary antibody overnight at 4 °C, washed with PBS with Tween 20 and probed with secondary antibody for 1 h at room temperature. The primary antibodies used were: VSNL1 (1:1,000; Millipore); DGKB (1:1,000; Thermo Fisher Scientific); β-actin (1:2,000; Sigma-Aldrich); BCL2L2 (1:1,000; OriGene). Mouse brain samples were dissected, washed in PBS and snap-frozen in liquid nitrogen. Samples were homogenized in 0.5% sarkosyl buffer, and sarkosyl-soluble and sarkosyl-insoluble fractions were separated. Western blots were probed with either total tau (Ab-3 antibody; Invitrogen) or phospho-tau (AT8 antibody, pS202/pT205; Invitrogen).

Luciferase assay. HEK 293T cells were plated on poly-L-ornithine-coated 96-well plates. When 70–80% confluent, cells were transfected with pmirGLO Dual-Luciferase miR Target Expression Vector (Promega Corporation) containing 950 pb target 3′-UTR (centered around the proposed miR-203 binding site) and 20 nM mimic (Dharmacon) using lipofectamine 2000 (Thermo Fischer Scientific); 24–48 h after transfection, Dual-Glo Luciferase Assay (Promega) was used to measure both firefly-luciferase- and *Renilla*-luciferase-mediated luminescence with the BioTek Synergy 2 microplate reader (1 s integration time, 100 sensitivity). Firefly luciferase luminescence was normalized to *Renilla* luciferase luminescence to control for transfection efficiency. Samples treated with miR-203 mimic were normalized to samples treated with scrambled mimic (control).

CMAP analysis. The top 300 salmon and turquoise hub genes (according to descending kME values) were used as input for the CMAP database (see URLs). This signature was used to query drugs or small molecules; the similarity between this signature and more than 7,000 expression profiles for 1,309 compounds (reference signatures) in the CMAP database were evaluated[80]. The enrichment of both salmon and turquoise module hub genes in the profiles of each treatment instance were estimated with a metric based on the Kolmogorov–Smirnov statistic (a nonparametric, rank-based, pattern-matching strategy), as described by Lamb et al.[80], and combined to produce a 'connectivity score.' Mean connectivity scores across several cell lines were then ranked by increasing order of connectivity. The gene expression data of the top-scoring drug, scriptaid, was extracted from the CMAP database and used for finding genes differentially affected by drug treatment.

Generation of the human iNgn2 neurons and compound treatment. The control 8330-8-RC1 and tau-A152T 19-5-RC6 neural progenitor cell (NPC) lines (derived from 8330-8 and 19-5 iPSCs; generation of these iPSC cell lines has been previously described[81–83]) were stably transduced with an inducible neurogenin-2 (iNGN-2) construct containing puromycin and blasticidin selection markers and a transactivator construct (derivation method described in Cheng et al.[81]) resulting in the iNGN-2-NPC stable cell lines. On day 0, each of the iNGN-2-NPC cell lines was plated at 9×10^5 cells per well into 6-well plates precoated with 20 μg ml^{-1} poly-L-ornithine, and 5 μg ml^{-1} laminin (Sigma-Aldrich) in neural medium (48% Gibco Neurobasal Medium, 48% Gibco DMEM/F-12 (Thermo Fisher Scientific), 1% Gibco B-27 serum-free supplement (Thermo Fisher Scientific), 0.5% Gibco N-2 supplement (Thermo Fisher Scientific), 0.75% Gibco GlutaMAX (Thermo Fisher Scientific), 1% Gibco penicillin–streptomycin (Thermo Fisher Scientific), 0.5% Gibco MEM nonessential amino acids solution (Thermo Fisher Scientific), 50 μM 2-mercaptoethanol (BioRad), 0.2% BSA (Sigma-Aldrich), 2 μg ml^{-1} doxycycline (Clontech), 10 ng ml^{-1} brain-derived neurotrophic factor (Peprotech), and 10 ng ml^{-1} neurotrophin-3 (Peprotech) to start neural induction. The cells were refed every other day with half replacement of the neural medium, with 1 μg ml^{-1} puromycin (Sigma-Aldrich) added on day 2 and 4, and cytosine arabinoside (Sigma-Aldrich) on day 6. Between days 13 and 14, the cells were treated for 24 h with either 0.05% DMSO (vehicle control), 500 nM, 1 μM or 2.5 μM SAHA in neural medium minus the growth factors and doxycycline. After the 24 h treatment, the 14-day iNGN-2 neurons were collected in TRIzol reagent (Invitrogen), with each replicate collected from two wells and stored at −80 °C.

FACS sorting of adult mouse neurons. Cortical cell suspensions from adult mouse neurons were labeled with live cell marker DRAQ5 (1 μl per 1 ml of cell suspension; Thermo Fisher Scientific) and dead cell marker NucBlue (2 drops ml^{-1} of cell suspension). The cells were FACS-sorted on a Becton Dickinson FACS Aria cell sorter gating for DAPI$^-$/DRAQ5$^+$/GFP$^+$ cells. For each sample, a maximum of 1,000 cells were isolated and directly collected in 100 μl of RA1 buffer with 2 μl TCEP; low-mass RNA was isolated with on column DNase digestion using a NucleoSpin RNA XS kit according to the manufacturer's protocol.

Reporting summary. Further information on research design is available in the Nature Research Reporting Summary linked to this article.

Data availability

miRNA-seq and mRNA-seq data from TPR50 tau mice, microarray data on PS19 hippocampus, microarray data on overexpression of miR-203 in vitro, RNA-seq on sorted mouse neurons and RNA-seq data with SAHA are available from the NCBI Gene Expression Omnibus database under Gene Expression Omnibus accession number GSE90696. Human FTD miRNA-seq and mRNA-seq data are available from https://www.synapse.org/#!Synapse:syn7818788. Human UPenn FTD Proteomics data are available from https://www.synapse.org/#!Synapse:syn9884357. The custom code used for the analysis can be accessed using this link in github: https://github.com/dhglab/Identification-of-evolutionarily-conserved-gene-networks-mediating-neurodegenerative-dementia

References

52. Schroeder, A. et al. The RIN: an RNA integrity number for assigning integrity values to RNA measurements. *BMC Mol. Biol.* **7**, 3 (2006).
53. Wes, P. D. et al. Tau overexpression impacts a neuroinflammation gene expression network perturbed in Alzheimer's disease. *PLoS ONE* **9**, e106050 (2014).
54. Srinivasan, K. et al. Untangling the brain's neuroinflammatory and neurodegenerative transcriptional responses. *Nat. Commun.* **7**, 11295 (2016).
55. Chishti, M. A. et al. Early-onset amyloid deposition and cognitive deficits in transgenic mice expressing a double mutant form of amyloid precursor protein 695. *J. Biol. Chem.* **276**, 21562–21570 (2001).
56. Matarin, M. et al. A genome-wide gene-expression analysis and database in transgenic mice during development of amyloid or tau pathology. *Cell Rep.* **10**, 633–644 (2015).
57. Lui, H. et al. Progranulin deficiency promotes circuit-specific synaptic pruning by microglia via complement activation. *Cell* **165**, 921–935 (2016).
58. Kim, D. et al. TopHat2: accurate alignment of transcriptomes in the presence of insertions, deletions and gene fusions. *Genome Biol.* **14**, R36 (2013).
59. Li, H. et al. The Sequence Alignment/Map format and SAMtools. *Bioinformatics* **25**, 2078–2079 (2009).
60. Anders, S., Pyl, P. T. & Huber, W. HTSeq: a Python framework to work with high-throughput sequencing data. *Bioinformatics* **31**, 166–169 (2015).
61. Conesa, A. et al. A survey of best practices for RNA-seq data analysis. *Genome Biol.* **17**, 13 (2016).
62. Robinson, M. D., McCarthy, D. J. & Smyth, G. K. edgeR: a Bioconductor package for differential expression analysis of digital gene expression data. *Bioinformatics* **26**, 139–140 (2010).
63. Risso, D., Schwartz, K., Sherlock, G. & Dudoit, S. GC-content normalization for RNA-seq data.*BMC Bioinformatics* **12**, 480 (2011).
64. Dobin, A. et al. STAR: ultrafast universal RNA-seq aligner. *Bioinformatics* **29**, 15–21 (2013).
65. Hansen, K. D., Irizarry, R. A. & Wu, Z. Removing technical variability in RNA-seq data using conditional quantile normalization. *Biostatistics* **13**, 204–216 (2012).
66. Friedländer, M. R., Mackowiak, S. D., Li, N., Chen, W. & Rajewsky, N. miRDeep2 accurately identifies known and hundreds of novel microRNA genes in seven animal clades. *Nucleic Acids Res.* **40**, 37–52 (2012).
67. Love, M. I., Huber, W. & Anders, S. Moderated estimation of fold change and dispersion for RNA-seq data with DESeq2. *Genome Biol.* **15**, 550 (2014).
68. Li, A. & Horvath, S. Network neighborhood analysis with the multi-node topological overlap measure. *Bioinformatics* **23**, 222–231 (2007).
69. Hawrylycz, M. et al. Canonical genetic signatures of the adult human brain. *Nat. Neurosci.* **18**, 1832–1844 (2015).
70. Zambon, A. C. et al. GO-Elite: a flexible solution for pathway and ontology over-representation. *Bioinformatics* **28**, 2209–2210 (2012).
71. Csardi, G. & Nepusz, T. The igraph software package for complex network research. *nterJournal,Complex Systems* **1695**, 1–9 (2006).
72. Zhang, Y. et al. An RNA-sequencing transcriptome and splicing database of glia, neurons, and vascular cells of the cerebral cortex. *J. Neurosci.* **34**, 11929–11947 (2014).
73. Langfelder, P., Luo, R., Oldham, M. C. & Horvath, S. Is my network module preserved and reproducible? *PLoS Comput. Biol.* **7**, e1001057 (2011).
74. Rivals, I., Personnaz, L., Taing, L. & Potier, M. C. Enrichment or depletion of a GO category within a class of genes: which test? *Bioinformatics* **23**, 401–407 (2007).
75. Benjamini, Y. & Hochberg, Y. Controlling the false discovery rate: a practical and powerful approach to multiple testing. *J. R. Stat. Soc. Series B Methodol.* **57**, 289–300 (1995).
76. Grimson, A. et al. MicroRNA targeting specificity in mammals: determinants beyond seed pairing. *Mol. Cell* **27**, 91–105 (2007).
77. Rossin, E. J. et al. Proteins encoded in genomic regions associated with immune-mediated disease physically interact and suggest underlying biology. *PLoS Genet.* **7**, e1001273 (2011).

78. Voineagu, I. et al. Transcriptomic analysis of autistic brain reveals convergent molecular pathology. *Nature* **474**, 380–384 (2011).
79. Cox, J. et al. Accurate proteome-wide label-free quantification by delayed normalization and maximal peptide ratio extraction, termed MaxLFQ. *Mol. Cell Proteomics* **13**, 2513–2526 (2014).
80. Lamb, J. et al. The Connectivity Map: using gene-expression signatures to connect small molecules, genes, and disease. *Science* **313**, 1929–1935 (2006).
81. Cheng, C., Fass, D. M., Folz-Donahue, K., Macdonald, M. E. & Haggarty, S. J. Highly expandable human iPS cell–derived neural progenitor cells (NPC) and neurons for central nervous system disease modeling andhigh-throughput screening. *Curr. Protoc. Hum. Genet.* **92**, 21.8.1–21.8.21 (2017).
82. Almeida, S. et al. Induced pluripotent stem cell models of progranulin-deficient frontotemporal dementia uncover specific reversible neuronal defects. *Cell Rep.* **2**, 789–798 (2012).
83. Biswas, M. H. U. et al. MMP-9 and MMP-2 contribute to neuronal cell death in iPSC models of frontotemporal dementia with MAPT mutations. *Stem Cell Reports* **7**, 316–324 (2016).

nature research

Corresponding author(s): Daniel H. Geschwind

Reporting Summary

Nature Research wishes to improve the reproducibility of the work that we publish. This form provides structure for consistency and transparency in reporting. For further information on Nature Research policies, see Authors & Referees and the Editorial Policy Checklist.

Statistical parameters

When statistical analyses are reported, confirm that the following items are present in the relevant location (e.g. figure legend, table legend, main text, or Methods section).

n/a	Confirmed	
☐	☒	The exact sample size (*n*) for each experimental group/condition, given as a discrete number and unit of measurement
☐	☒	An indication of whether measurements were taken from distinct samples or whether the same sample was measured repeatedly
☐	☒	The statistical test(s) used AND whether they are one- or two-sided *Only common tests should be described solely by name; describe more complex techniques in the Methods section.*
☐	☒	A description of all covariates tested
☐	☒	A description of any assumptions or corrections, such as tests of normality and adjustment for multiple comparisons
☐	☒	A full description of the statistics including central tendency (e.g. means) or other basic estimates (e.g. regression coefficient) AND variation (e.g. standard deviation) or associated estimates of uncertainty (e.g. confidence intervals)
☐	☒	For null hypothesis testing, the test statistic (e.g. *F*, *t*, *r*) with confidence intervals, effect sizes, degrees of freedom and *P* value noted *Give P values as exact values whenever suitable.*
☒	☐	For Bayesian analysis, information on the choice of priors and Markov chain Monte Carlo settings
☒	☐	For hierarchical and complex designs, identification of the appropriate level for tests and full reporting of outcomes
☐	☒	Estimates of effect sizes (e.g. Cohen's *d*, Pearson's *r*), indicating how they were calculated
☐	☒	Clearly defined error bars *State explicitly what error bars represent (e.g. SD, SE, CI)*

Our web collection on statistics for biologists may be useful.

Software and code

Policy information about availability of computer code

Data collection	R package WGCNA was used for network analysis. GOElite package was used for Gene-ontology and KEGG pathway enrichment. Tophat, STAR were used for alignment and HT-Seq count was used for count-level calculation. In addition,
Data analysis	Custom codes used for the study can be accessed using the link : https://github.com/dhglab/Identification-of-evolutionarily-conserved-gene-networks-mediating-neurodegenerative-dementia

For manuscripts utilizing custom algorithms or software that are central to the research but not yet described in published literature, software must be made available to editors/reviewers upon request. We strongly encourage code deposition in a community repository (e.g. GitHub). See the Nature Research guidelines for submitting code & software for further information.

Data

Policy information about availability of data

All manuscripts must include a data availability statement. This statement should provide the following information, where applicable:

- Accession codes, unique identifiers, or web links for publicly available datasets
- A list of figures that have associated raw data
- A description of any restrictions on data availability

miRNA- and mRNA-seq data from TPR50 Tau mice, microarray data on PS19 hippocampus, microarray data on overexpression of miR-203 in vitro, RNA-seq on

sorted mouse neurons, and RNA-seq data with SAHA available at the NCBI Gene Expression Omnibus database under Gene Expression Omnibus accession number #GSE90696. Human FTD miRNA- and mRNA-seq data is available at https://www.synapse.org/#!Synapse:syn7818788. Human UPenn FTD Proteomics data is available at https://www.synapse.org/#!Synapse:syn9884357.

Field-specific reporting

Please select the best fit for your research. If you are not sure, read the appropriate sections before making your selection.

☒ Life sciences ☐ Behavioural & social sciences ☐ Ecological, evolutionary & environmental sciences

For a reference copy of the document with all sections, see nature.com/authors/policies/ReportingSummary-flat.pdf

Life sciences study design

All studies must disclose on these points even when the disclosure is negative.

Sample size	No formal approach was used to compute sample size, however previous work in the lab had indicated that our sample size would be sufficient to identify significant changes. Additionally, the accuracy of RNA-seq is contigent on the methodology used. Notably, at current sample sizes in gene expression studies, there are always more significant findings as sample size is increased but they are of diminishingly small effect sizes. Finally, in large scale gene expression studies, each gene differs in variability across samples and power depends on this variability, sample size, RNA quantification methodology, and the distribution of relevant covariates. This would require extensive modeling with many assumptions to project sample sizes and power. We therefore chose to demonstrate reproducibility of our data in independent samples, which empirically demonstrates that our study is reasonably well-powered.
Data exclusions	For gene-expression studies, outlier samples were excluded using a quality z-score which was calculated for each sample, and samples with low quality (Z > 2 or Z < -2) were identified as outlier and removed from further analysis.
Replication	All attempts for replicating the findings in the study were successful and all the replicates are reported in the study.
Randomization	For gene-expression studies, samples were randomized across dissection, RNA extraction, library preparation, and sequencing/microarray as described in the Extended methods section of the supplemental information.
Blinding	Investigators were blinded during dissection, RNA extraction, and sequencing/microarray to all metadata information about the samples. Investigators were also blinded for mouse in vitro experiments including viral injections and histopathology.

Reporting for specific materials, systems and methods

Materials & experimental systems

n/a	Involved in the study
☐	☒ Unique biological materials
☐	☒ Antibodies
☒	☐ Eukaryotic cell lines
☒	☐ Palaeontology
☐	☒ Animals and other organisms
☐	☒ Human research participants

Methods

n/a	Involved in the study
☒	☐ ChIP-seq
☐	☒ Flow cytometry
☒	☐ MRI-based neuroimaging

Unique biological materials

Policy information about availability of materials

Obtaining unique materials	Human postmortem brain samples used in the study were obtained from appropriate brain banks which are mentioned in the methods section. All other unique materials are available from the authors.

Antibodies

Antibodies used	Phospho-tau (Ser202, Thr205) AT8 clone (Thermo Fisher, #MN1040), Glial Fibrilary Acid protein (GFAP, Dako, #Z033429), Iba-1 (Wako, #019-19741), total tau - Thermo Fisher, #KHB0041), pT231 tau (Thermo Fisher, #KHB8051), VSNL1 (Millipore #MABN762), DGKB (ThermoScientific #PA5-15416), a-actin (Sigma, #A1978), BCL2L2 (Origene, #TA302168), AT8 antibody pS202/ pT205(Thermo Fisher, #MN1020), Abeta-3 antibody(Thermo Fisher, #RB-1429).

Validation	All antibodies are well-validated by the manufacturer and are widely used in the scientific community. In addition, we observed expected bands and strong signal in mouse and human cell lines.

Animals and other organisms

Policy information about studies involving animals; ARRIVE guidelines recommended for reporting animal research

Laboratory animals	C57Bl/6J, Tg4510 and TPR50 Tau transgenic mice were used in the study. While both males and females were used for TPR50 mice, only male mice were used for C57BL/6J wild-type and Tg4510 Tau tg mice. Mice with ages between 4-52 weeks were used for all the experiments
Wild animals	Study did not involve wild animals
Field-collected samples	Study did not involve field-collected samples

Human research participants

Policy information about studies involving human research participants

Population characteristics	Postmortem human brain samples from human AD and FTD and control cases (both male and female) range from 50 years to 90 + years with median age of 70 years.
Recruitment	Only human postmortem brain samples were used in the study and were obtained from appropriate brain banks which are mentioned in the methods section.

Flow Cytometry

Plots

Confirm that:

☒ The axis labels state the marker and fluorochrome used (e.g. CD4-FITC).

☒ The axis scales are clearly visible. Include numbers along axes only for bottom left plot of group (a 'group' is an analysis of identical markers).

☒ All plots are contour plots with outliers or pseudocolor plots.

☒ A numerical value for number of cells or percentage (with statistics) is provided.

Methodology

Sample preparation	Frontal cortex of adult male mice was dissected in ice-cold Hibernate A-lacking calcium (BrainBits; HA-Ca). Tissue was roughly chopped in HA-Ca, moved to 15mL Falcon tube and incubated in 5ml of activated papain (Worthington; LK003178; resuspended in HA-Ca) in the presence of DNase I for 30min at 37˚C with continuous agitation. Papain digested tissue was triturated and cell debris was removed using ovomucoid (Worthington; LK003182; resuspended in HA-Ca) discontinuous density gradient centrifugation. The cell pellet was resuspended in 1.8mL Hibernate A-low fluorescence (BrainBits; HA-LF) to create a mononuclear cell suspension. To further reduce the amount of debris, the Miltyni myelin removal kit was used. Briefly, 200uL myelin removal beads (Miltyni; 130-096-733) were added to the cell suspension, incubated at 4˚C for 15 minutes, 2mL of HA-LF was added and the cell suspension was centrifuged at 300g for 10 minutes at 4˚C. The supernatant was aspirated and the pellet was resuspended in 1mL of HA-LF and applied to prepared LS columns (Miltyni; 130-042-401). Flow-through, as well as two 1mL washes with HA-LF, were collected, centrifuged at 600g for 5min at 4˚C and resuspended in 750uL HA-LF. Myelin depleted samples were labeled with live cell marker DRAQ5 (Fisher; 6225; 1uL/1mL of cell suspension) and dead-cell marker NucBlue® (Invitrogen; R37606; 2 drops/mL of cell suspension).
Instrument	BD Aria II SORP
Software	FACSDiva software Version 8.0.0
Cell population abundance	The GFP positive cells were sorted using 4-way purity and the FACS efficecy was always maintained higher than 85%. Post-sorted GFP positive cells were confirmed under microscope for cell morphology and GFP fluorescence.
Gating strategy	After setting the initial gate for FSC (Gate P1) and SSC (Gate P2) and both (Gate P3) based on previous experiments with adult mouse cortex, we further gated for DAPI -ve and DRAQ5 positive gates to get "live" cells (Gate P4). Gate P4 was then sorted for GFP positive fraction based on fluorescent intensity

☒ Tick this box to confirm that a figure exemplifying the gating strategy is provided in the Supplementary Information.